IMPROVING THE QUANTIFICATION ACCURACY OF Tc-99m MIBI DUAL-PHASE PARATHYROID SPECT/CT: A MONTE CARLO SIMULATION STUDY

by

Bahadır Aytaç

B.S., in Electrical-Electronics Engineering, Gazi University, 2021

Submitted to the Institute of Biomedical Engineering
in partial fulfillment of the requirements
for the degree of
Master of Science
in
Biomedical Engineering

Boğaziçi University
2023

ACKNOWLEDGMENTS

This has been a long and arduous journey and words can't express my gratitude to my advisor Prof. Dr. Albert Güveniş for his patience and leadership throughout. I also would like to express my deepest appreciation to the defense committee, for without their expertise and input this journey would not be possible. Additionally, I would like to thank Celal Bilir and Senay Akbulut for their insights and expertise.

I would like to thank my classmates and friends who without their feedback, companionship, and wisdom, I could not undertaken this journey. Thanks should also go to the academic staff, researchers, and general staff within the institute who impacted and inspired me.

Lastly, I would like to thank my family for their support and belief. Which kept my spirits and motivation up to continue during this work.

ACADEMIC ETHICS AND INTEGRITY STATEMENT

I, Bahadır Aytaç, hereby certify that I am aware of the Academic Ethics and Integrity Policy issued by the Council of Higher Education (YÖK) and I fully acknowledge all the consequences due to its violation by plagiarism or any other way.

Name :

Signature:

Date:

ABSTRACT

IMPROVING THE QUANTIFICATION ACCURACY OF Tc-99m MIBI DUAL-PHASE PARATHYROID SPECT/CT: A MONTE CARLO SIMULATION STUDY

Quantitative parathyroid SPECT imaging is a technique used to assess primary hyperparathyroidism that may have potential in the identification and differentiation of parathyroid lesions as well as the estimation of disease severity. Studying the effect of data acquisition parameters on the quantification error is important for maximizing the accuracy of this diagnostic technique. In this study, we examine the effects of different data acquisition parameters, namely the type of collimator, scatter correction status, and reconstruction iteration number on the quantification accuracy using computer simulation. The SIMIND Monte Carlo Simulation and CASToR iterative reconstruction program was used to simulate a commercially available SPECT camera (Siemens Symbia Intevo Gamma Camera) with a crystal size of 29.55cm and 128x128 matrix size. A digital cylindrical phantom filled with water was constructed. A 0.36 cm radius spherical adenoma filled with a uniform 1MBq/cc Tc99m-Sestamibi was placed within the phantom. Low-Energy High Resolution (LEHR) and Low Energy Ultra High Resolution (LEUHR) collimator models are tested. Along with the presence of Scatter correction and differing iteration numbers (x16, x32). An image FOV-based calibration method was used to gather quantitative information and check against the input radioactivity. The presence of scatter correction is observed to cause a 15-20 percent relative improvement in quantification accuracy. The optimal number of iterations produced a 10 percent relative improvement. Overall, accuracies as good as 7 percent in estimated activity concentration could be observed. Thus showcasing that the optimization of parameters can provide a significant improvement in quantification accuracy.

Keywords: SPECT, Monte Carlo Simulation, Quantification, Hyperparathyroidism

ÖZET

Tc-99m MIBI İKİ AŞAMALI PARATROİT SPECT/CT'NİN KUANTİTATİF DOĞRULUĞUNUN ARTIRILMASI: BİR MONTE CARLO SİMÜLASYON ÇALIŞMASI

Kuantitatif paratiroid SPECT görüntüleme, birincil hiperparatiroidizmi değerlendirmekte kullanılan bir tekniktir ve paratiroid lezyonlarını tanımlanışı ve ayırt edilişi ile hastalık şiddetinin tahmini konusunda potansiyele sahip olabilir. Veri toplama parametrelerinin kuantitatif hata üzerindeki etkisini incelemek, bu tanısal tekniklerin doğruluğunu maksimize etmek açısından önemlidir. Bu çalışmada, bilgisayar simülasyonu kullanarak farklı veri toplama parametrelerinin, yani kollimatör türü, saçılma düzeltme durumu ve rekonstrüksiyon iterasyon sayısının kuantitatif doğruluk üzerindeki etkileri incelenmiştir. SIMIND Monte Carlo Simülasyonu ve CASToR yinelemeli rekonstrüksiyon programı, 29.55 cm kristal boyutu ve 128x128 matris boyutuna sahip ticari bir SPECT kamera (Siemens Symbia Intevo Gamma Kamera) simüle etmek için kullanılmıştır. Su ile doldurulmuş dijital silindirik bir fantom oluşturulmuştur. Fantom içine, 0.36 cm yarıçaplı, 1MBq/cc birim Tc99m-Sestamibi radyoaktivite ile doldurulmuş bir küresel adenoma yerleştirilmiştir. Düşük Enerji Yüksek Çözünürlük (LEHR) ve Düşük Enerji Ultra Yüksek Çözünürlük (LEUHR) kollimatör modelleri test edilmiştir. Ayrıca, saçılma düzeltmesi varlığı ve farklı iterasyon sayıları (x16, x32) incelenmiştir. Nicel bilgileri toplamak için bir görüntü FOV tabanlı kalibrasyon yöntemi kullanılmış ve girdi radyoaktivite ile karşılaştırılmıştır. Saçılma düzeltmesinin varlığı, kuantitatif doğruluğunda %15-20 oranında bir iyileşme sağlamıştır. Optimal iterasyon sayısı, %10 oranında bir iyileşme üretmiştir. Genel olarak, tahmini aktivite konsantrasyonunda %7'ye kadar olan doğruluklar gözlemlenebilir. Görüldüğü üzere parametrelerin optimize edilmesi, kuantitatif doğruluğunda önemli bir iyileştirme sağlayabilir.

Anahtar Sözcükler: SPECT, Monte Carlo Simülasyonu, Kuantitatif İnceleme, Hiperparatiroitizm

TABLE OF CONTENTS

LIST OF FIGURES

LIST OF TABLES

LIST OF SYMBOLS

A	The system matrix during reconstruction process
A_{ij}	Probability of a photon from voxel j being found in pixel i.
f_x	Activity distribution voxels of the image
p	Detector pixels
x_i	Distance travelled by a photon during attenuation
I_0	Incident photon before attenuation
A_{mean}	Mean activity over the acquisition
N_x	Number of counts per cc
S_x	Calibration factor
μ_i	Attenuation coefficient of a particular tissue
ΔT_{acq}	Acqusition time during imaging

LIST OF ABBREVIATIONS

LEHR	Low Energy High Resolution
LEUHR	Low Energy Ultra High Resolution
CASToR	Customizable Advanced Software for Tomography
PHPT	Primary Hyperparathyroidism
PTH	Parathyroid Hormone
VOI	Volume of Interest
UV	Ultra Violet
CZT	Cadmium-Zinc-Telluride
PMT	Photo-Multipler Tube
MLEM	Maximum Likelihood Expectation Maximization
OSEM	Ordered Subset Likelihood Maximization
CT	Computed Tomography
SPECT	Single Photon Emission Computed Tomography
TEW	Triple-Energy-Window
OLEM	Optimization Based Reconstruction Algorithms
NaI	Sodium Iodide
mm	Millimeter
Bq/cc	Becquerel per cc

1. INTRODUCTION

Primary hyperparathyroidism (PHPT) is among the most common endocrine disorders in the world. The disorder can cause the overproduction of parathyroid hormones (PTH) and an increase of plasma calcium levels in the blood [1]. It presents itself in the form of irregularities and over-release of PTH. Symptomatic representation of PHPT is commonly seen around the renal system and skeletal structures, with patients suffering from fragility in bones, renal nephrocalcinosis, and renal insufficiency. However, with the improvements in modern medicine and the ability to screen serum calcium levels, it is possible for physicians to gradually shift the PHPT presentation form from symptomatic to asymptomatic presentations [2]. Around 80% to 85% of hyperparathyroidism is caused by parathyroid adenomas, with primary parathyroid hyperplasia (15%) and parathyroid carcinoma (5%) less commonly linked with the disorder [1, 3]. Most patients exhibit adenomas on a single gland while about 20% percent of patients have multiple adenomas on their glands [4].

Under normal circumstances, parathyroids are too small to detect but PHPT causes the glands to increase in size resulting in an enlarged state that allows imaging [3]. Patients with enlarged glands are generally advised to be operated on for the removal of the adenoma. In contrast, for some patients who are not seen fit for surgical operation according to relevant guidelines, [5], physicians can follow more conservative approaches such as the newer less invasive surgical interventions [4].

Parathyroid glands are rather small (generally 5x3x1 mm [3]) and situated right behind the thyroid glands [6]. This makes imaging difficult. Sonography and Tc99m-Sestamibi scintigraphy are the imaging modalities used for imaging parathyroid glands [3]. Tc99m-Sestamibi is a known substance used in parathyroid imaging being absorbed by both the adenomas and the thyroid glands. The substance then washes off the thyroid glands and provides a good vision of the adenomas in parathyroids.

1.1 Quantification

Quantification of a medical image means gathering not only visual but also numeric information on biological structures such as the concentration of radioactive material within a certain biological structure in units of kilo becquerels per cubic centimeter [7]. With the addition of iterative imaging methods that allow corrections during reconstruction, quantitative imaging has become more prevalent in SPECT imaging. This allows the user to further understand the properties of pathologies. With the adaptation of CT imaging systems to SPECT, the availability of correction methods for various effects have become available, thus making SPECT/CT suitable for quantitative emission imaging. Therefore, allowing researchers and physicians alike to observe in vivo activity distribution in absolute units [8].

Some studies have examined the benefits of quantification. [9] uses quantification to observe the effect of delay in Tc99m SPECT/CT imaging of secondary hyperparathyroidism patients. Another study on thyroid imaging [10] found that quantitative SPECT/CT measurements were more accurate than the thyroid uptake system (TUS). There are articles in the literature that describe quantitative imaging as one of the most promising practices in nuclear medicine [10, 11, 12, 13].

In the case of an adenoma, quantification allows the observation of not only the radioactivity level, but also properties such as size, shape, position, and volume in a much more precise way. Furthermore, it is possible to assess disease severity [14, 15].

The detection and quantitative analysis of parathyroid adenomas is a studied field that contains many approaches. Namely, [16] used particle swarm optimization with random neighbor topology to achieve 3% voxel size with heavily reduced processing times. [9, 11, 17, 18] have used quantitative methods to gather information on optimal timing, standard uptake by time, and washout of radionuclides during imaging. [19] have employed a semi-quantitative method to analyze the degree of hyperplasia of the parathyroid gland pre-operation. While [20] were able to localize adenomas within 19mm of accuracy. Making the quantitative techniques a viable option for non-invasive analysis. [21] has used quantitative analysis of parathyroid imaging to test the co-registration combinations of the early and delayed SPECT/CT scans to achieve the most viable pair along with operator variability. [12] has successfully used quantitative analysis in the localization of adenomas.

The consensus is that accurate acquisition of quantitative data is a critical step in dosimetry and personalized treatment planning in nuclear medicine. For dosimetry an accurate representation of the distribution of radiopharmaceuticals is critical, thus underlining the growing importance of absolute quantification [8]. However, inaccurate calculation of quantitative measures can cause mistreatment and potential adverse side effects [22]. Additionally, quantification in nuclear imaging is still a practice that relies on parameter adjustment and allows only the cross-calibration between the SPECT and the dosimetry. The current status makes standardization of quantification a need since the differences in parameters such as reconstruction algorithm, calibration, and correction method are prone to creating local biases within different systems [8].

1.1.1 Parameters That Can Affect Quantification

1.1.1.1 Collimator Resolution. The distant-dependent resolution does not influence the sensitivity factor in relation to the source to camera distance. There is an inverse square relation between detected photons passing through a certain hole and emitted photons. But as the source is moved away from the camera, the chance for the photons to pass through adjunct holes increases squared to the source-camera distance and cancels out the inverse square effect. Therefore, the source-to-camera distance does not affect sensitivity [23]. However, the spread and distribution of the counts during the imaging can degrade contrast and make the imaging of smaller VOI harder. This spread is called a point spread function and it is described through a Gaussian function that is distance dependent.

1.1.1.2 Septal Penetration and Back-Scattering.

Collimators have a limitation of maximum energy as the collimators are designed with many demands in mind, such as max sensitivity, high spatial resolution, and efficiency in weight and cost. Thus, for some high-energy nuclides (131I, 90Y), the photons emitted from the source will have a probability of penetrating the collimator walls, causing serious degradation in quality. This results in lower spatial resolution and higher count rate which affects the calibration process during quantification [23].

1.1.1.3 Dead Time Effects.

When imaging with a high-activity source there is a chance that the scintillation cameras cannot distinguish between certain events. Most systems can be categorized into two systems[23]:

1. **Paralyzable systems:** In these systems, events can cause dead time effects regardless of their status. This means that the system cannot detect any new events while it is processing an existing event.
2. **Nonparalyzable systems:** In these systems, events that occur during dead time are ignored. This means that the system can continue to detect new events even while it is processing an existing event.

In other words, a non-paralyzable system does not stop detecting events when it is already processing another event. This is in contrast to a paralyzable system, which will stop detecting events until it has finished processing the current event.

Dead time is the period of time after an event has been detected during which the system is unable to detect another event. This is typically due to the time it takes for the system to process the first event. In a nonparalyzable system, events that occur during dead time are ignored. This means that the system will not record those events.

1.2 SPECT

1.2.1 Architecture and Hardware

Since the introduction of radioactive tracers into the medical sciences, there has been a need and desire to visualize and quantify the uptake and distribution of these tracers. In 1957, Hal Anger tackled this problem by developing the gamma camera [24]. But it wasn't until the 1960s and 70s that SPECT became commercially available in a wide manner [25]. While SPECT/CT became commercially available in the 1990s [26].

A classic gamma camera consists of three main components: A collimator, a scintillator, and an array of photomultiplier tubes(PMTs), as seen in Figure 1.1. The collimator consists of a collection of parallel holes separated by a highly attenuating septa material. This allows the collimator to filter parallel photonic emissions onto the detector and allow a projection of the object(Figure 1.2) being imaged. Unfortunately, since the collimator holes are neither infinitely long nor infinitely narrow, this results in a certain acceptance angle where any emission can pass through [24].

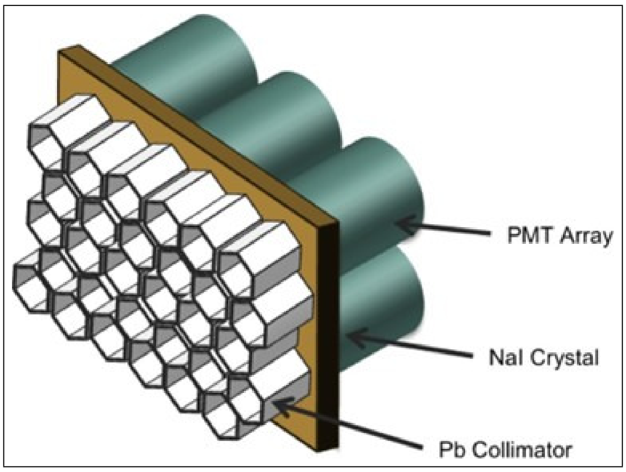

Figure 1.1 Simplified representation of the gamma camera structure [23].

Currently, dual detector head cameras are the norm in clinical practice, due to the advantageous balance they provide between photon sensitivity and operation cost. The SPECT/CT systems also include a gantry and a patient bed for patient and detector positioning. While computers and various electronics provide acquisition, reconstruction, and post-processing [8, 24].

In multimodal systems such as SPECT/CT the modalities are generally installed sequentially. Thus allowing the system to attach morphological information to the radiopharmaceutical uptake[8]. The operations of the modalities are also carried out sequentially such as firstly taking the SPECT image and then the CT. The SPECT employs co-planar imaging with adaptable rotation times and dose-optimized acquisition. While CT is carried out with multi-sliced cone beam systems [8, 26].

The modern SPECT detectors still resemble the original Anger design[8]. A projection function is obtained by the absorptive collimators located in front of the detector. The high-energy gamma photons are absorbed by the scintillation crystal (typically NaI) and then emitted as low-energy ultraviolet photons further into photomultipliers. Here the low-energy UV photons are transformed into electronic signals. From these electronic signals, through signal analysis and pulse height spectrometry, the location and the energy level of the incident photons are calculated [8, 24].

The spatial resolution of a SPECT image is not only dependent on the collimator and the acquisition geometry but also on the detector limitations. The intrinsic resolution of a detector is defined as the maximum spatial resolution that the detector can achieve. The intrinsic spatial resolution could be affected by the characteristics of the imaged radiopharmaceutical and the scintillation crystals parameters [8]. Typically, an intrinsic resolution of 3-5mm could be achieved in the commercially available SPECT systems.

Semiconductors can convert gamma radiation directly into electrical signals, which is faster than the standard scintillation crystal conversion. The semiconductor material currently being used for this purpose is Cadmium-Telluride and Cadmium-Zinc-Telluride(CZT). When paired with favorable collimation and geometry the CZT detectors have shown a considerable improvement over NaI. Studies show that CZT detectors show improvements in clinical areas such as shorter acquisition times(6min) and lower patient dose(1.15mSv) with similar image quality[22], [23][27, 28]. To learn more indepth about these experiments and CZT detector comparison, the reader can consult the review compiled by [8].

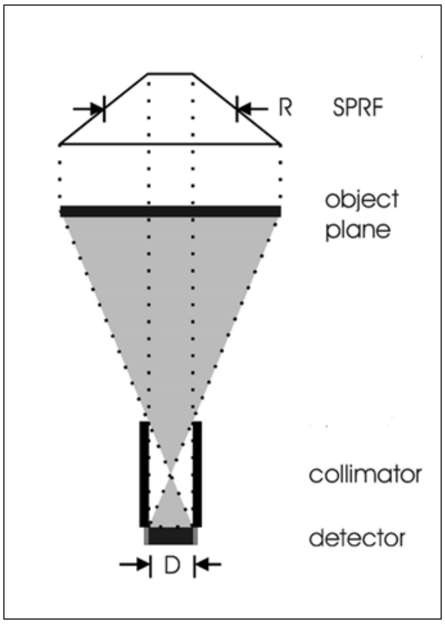

Figure 1.2 Showing the spatial resolution of a collimator with resolution R is defined as the FWHM of the single pixel response function. Adapted from [29].

1.2.2 Recontruction

Iterative reconstruction is currently the standard reconstruction technique in SPECT studies. It allows the use of correction and improvement techniques within the image processing chain. With improvement in this field, an even more advanced integration of SPECT and CT data is available, which means a better integration of morphological data with high spatial resolution and radiopharmaceutical information [8]. Most iterative reconstruction techniques rely on mathematical models that assume the relation between the image vector f(Activity distribution voxels) and the projection data vector p(Detector pixels) being dependent on a system matrix A, where each element A_{ij} of the system matrix A is defined as the probability of a photon originating from voxel j being found in pixel i.

$$A * f = p \tag{1.1}$$

The most common iteration algorithms are Maximum Likelihood Expectation Maximization (MLEM) and its accelerated version, Ordered Subset Expectation Maximization (OSEM). MLEM is based on the fact that image F consists of Poisson random variables and the maximization of the likelihood of the observed data [30]. Within the MLEM algorithm, we consider that image $f \subset R_n$, system matrix $A \subset R_{mxn}$, and measurements $p \subset R_n$. The image f can be recovered using maximum likelihood estimation solving an optimization program [31].

$$\begin{gathered}\text{Minimize } f_x \\ \text{Subject to } X > 0\end{gathered}$$

The mathematical rule of the MLEM algorithm is given in the Eq. 1.2.

$$f_n^{new} = \frac{f_n^{old}}{\sum_l a_{ln}} \sum_m a_{mn} \frac{pm}{\sum_k a_{mk}(f_k^{old})} \tag{1.2}$$

1.2.3 Correction Algorithms

Single photon emission computed tomography (SPECT) visualizes the radioactivity distribution across the human body on a field of view (FOV). Traditionally SPECT is seen as a qualitative imaging technique that has low special resolution and high noise in regions of interest [7, 4]. Since the recent development of iterative reconstruction algorithms, SPECT has joined others as a quantitative imaging modality that gives an accurate quantitative representation of radioactivity in the body. Corrections should be performed for maximum accuracy against naturally occurring physical phenomena, such as scattering and attenuation. These phenomena cause inaccuracies in radioactivity readings. Studies show that iterative reconstruction methods paired with correction methods can give much higher quantitative accuracy than their non-iterative (Filtered back projection etc.) counterparts [7, 32, 33].

1.2.3.1 Attenuation Correction. With the utilization of multimodality systems like SPECT/CT, it has become possible to tackle physical phenomena like the attenuation effect caused by the absorption and scattering of photons by the biological structures encountered. The main reason for attenuation in nuclear medicine is Compton scattering which causes the photon directions to change during travel. The attenuation effect, which causes underestimation of activity concentration, is generally more prevalent on the center of the object since the change of direction causes the photons that should have passed through the collimator to not be detected [26].

This misrepresentation could be corrected in SPECT/CT by using the CT image with the utilization of statistical iteration-based algorithms, such as MLEM and OSEM. Another matter to keep in mind is that the CT X-ray tubes generally output a collection of photons on an energy spectrum that includes both low and high-energy rays. From this spectrum low energy photons are more susceptible to attenuation. This effect is called the beam hardening effect which can be solved by filtering out the low-energy photons while being produced from the X-ray tube [34].

Below is an equation explaining the effect attenuation has on CT rays; where I_0 is the incident photon, I is the measured ray, μ_i the attenuation coefficient, and x_i traveled tissue distance with a certain attenuation coefficient.

$$I = I_0 e^{\sum_i \mu_i x_i} \tag{1.3}$$

There are several advantages to using CT images in attenuation correction, the main one being that since the CT provides a high photon flux, it reduces the statistical noise that occurs during the correction stage [34, 26].

1.2.3.2 Scatter Correction. Compton scattering is one of the most important factors in the interaction between radiation and material. When photons encounter a structure on their path during molecular imaging, there are a certain percentage of these photons (depending on the source) will change their direction. These interactions mainly happen within the source (the human body). The photons whose direction was diverted from their original location will cause misinformation in scintillation [35, 36]. Energy spectra of scattered and non-scattered(primary) photons in comparison to total energy spectra can be observed in Figure 1.3.

$$C_{primary} = C_{tot} - C_{scatter} \tag{1.4}$$

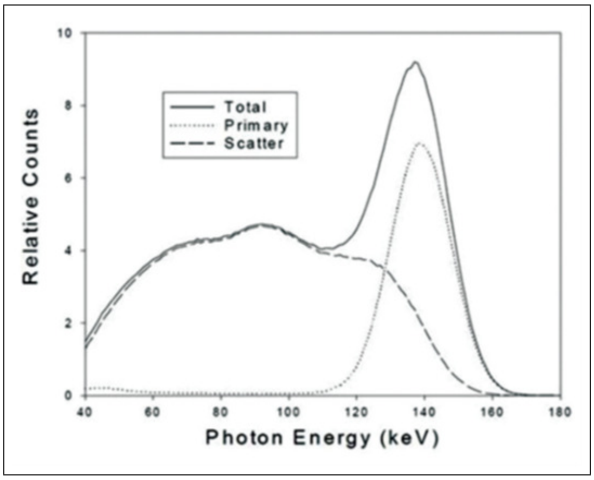

Figure 1.3 A demonstrative graphic of the event counts in their respective spectra [36].

In 1991 K. Ogawa introduced a new technique [37] to correct the artifacts and misinformation caused by the Compton scattering effect. The technique consisted of acquiring the counts from two sub-windows on each side of the main energy windows. This acquisition can be observed in Figure 1.4. The sub-window counts then would be subtracted to correct the effects of Compton scattering [36, 37].

$$C_{scat} = (\frac{C_{left}}{W_s} + \frac{C_{right}}{W_s})W_m/2 \tag{1.5}$$

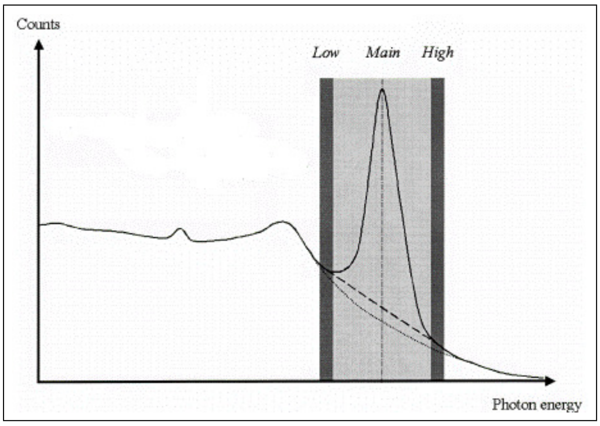

Figure 1.4 A graph of a typical TEW spectrum with high and low sub-windows with the main window in the center. Adapted from [38].

Where Wm is the width of the main window and Ws is the width of the sub-windows with Cleft, Cright being the sub-window counts.

1.2.3.3 Dead Time Correction. When talking about dead time effects it is important to understand the scintillation process. The one troublesome factor is that the scintillation light from NaI has a rather slow exponential emission decay, which means that the decaying energy from previous event energies can affect the registration of the current event [23]. This effect is called pulse pile-up. Correction for these effects is generally done through having an initially obtained reference count within the FOV either without the patient or with a phantom and checking the imaging count against the reference count values.

1.2.3.4 Partial Volume Effect. Within imaging, despite the developments toward increasing spatial resolution it is currently not possible to achieve perfect spatial resolution. Thus, making the imaging of small VOIs difficult. When activity counts are spread over a larger area than the source volume. Count registration of the source could be lost because of spill-out, similarly if there is a significant activity occurring just outside of VOI a spill-in of counts can occur [23].

1.3 Monte Carlo Simulation

Monte Carlo simulation is a mathematical method that is used to estimate the outcome of uncertain events. The method was invented by John von Neumann and Stanislaw Ulam during World War II to improve decision-making and was named after Monte Carlo, Monaco which is still known for its abundance of casinos and chance games. The Monte Carlo Simulation has been proven to be capable of analyzing complex systems and continuously executing various experiments with many parameters [39].

When performing a SPECT scan there is a large number of factors that need to be taken into consideration: detector properties, collimator models and randomly occurring physical events such as scattering and attenuation [40]. Furthermore, when trying to simulate a system such as SPECT, the ability to simulate randomly occurring events becomes paramount. Monte Carlo simulation is one such algorithm that allows the user to simulate these events and its use in Nuclear Medicine is well documented [41, 42]. Monte Carlo uses random sampling and a different number of probability density functions (pdf) to model, simulate, and predict complex systems [39].

As quantification becomes important for parathyroid SPECT/CT studies, there is a clinical need to identify the best acquisition and processing parameters that will yield the optimum accuracy. This study aims to address this need for the first time by using a Monte Carlo simulation platform for the Tc-99m MIBI dual-phase parathyroid SPECT/CT imaging protocol. Monte Carlo simulation allows the determination of optimal parameters while eliminating experimental errors and the expense and inconvenience of using physical systems.

2. METHODS

Compare results with previously obtained research findings:

- Use the previously validated cylindrical digital phantom[36] [43] and the Simind platform to enable multiple parameter testing. An illustration of images obtained using SIMIND is shown in Figures 3.1 and 3.2.
- Define processing acquisition parameters based on previous similar studies.
- Analysis of the results quantitatively, find the optimal parameters.
- Compare results with previously obtained research findings.

2.1 Imaging Modalities That Are Simulated

The dual-phase parathyroid Tc-99m-MIBI SPECT imaging protocol was used [44, 4, 45]. Specifically, Siemens Symbia Intevo Gamma Camera was chosen for the study. The Tables 2.1 and 2.2 give the specifications that belong to the gamma camera that is simulated.

Siemens Low-Energy High Resolution (LEHR) and Low-Energy ultra-high-resolution collimators have been used to see the effect of the collimator model on the quantification process (Table 2.2).

A digital cylindrical phantom has been selected for the study. The phantom was picked in a cylindrical shape to simulate the neck and upper torso area. The phantom has an 11cm cross-section and 30 cm height which is in line with previous anthropometric measurements of the neck and torso[46]. This gives us a chance to simulate the neck and upper torso area without an anthropomorphic phantom. The simulated phantom was filled with water. The pixel size for the phantom was chosen as 0.24mm according

Table 2.1
Spect camera specifications(in mm) in accordance with previous studies [4].

Camera Parameters	Value
Photon energy(keV)	140
Upper Window Threshold(keV)	147
Lower Window Threshold	133
Energy Resolution(140keV)	9.9%
Intrinsic Resolution(140keV)(cm)	0.3
Source Activity (MBq)	13629
Image Matrix Size	128x128
Number of SPECT Projections	48
SPECT Rotation(3=180)	3
Pizel size(cm)	0.24
Crystal Thickness	0.95
Crystal Half Length/Radius(cm)	29.55

Table 2.2
Siemens Collimator specifications. Sensitivity is set according to Tc99m[4].

Collimator	Hole length	Septal Thickness	Hole Diameter	Sensitivity	System Res.
LEHR	24.05	0.16	1.11	202	7.5
LEUHR	35.08	0.13	1.16	100	6

to previous studies [44, 4] while the entire phantom is sized 128x128x128 pixels. The adenoma is simulated as a uniform sphere with an offset 1.5cm from the center situated on the upper central portion of the cylinder, as seen in Figure 2.1. The sphere was sized 3x3x3 voxels, which corresponds to a radius of 0.36 cm. The sphere was filled with approximately 1MBq/cc.

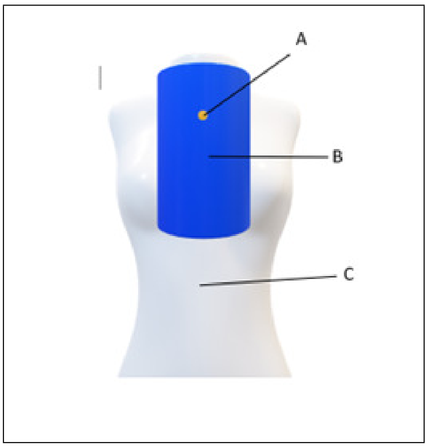

Figure 2.1 An approximate representation of the way the cylindrical phantom simulates the head and neck area. (A)The radioactive matter (B)The cylindrical phantom (C)A model human torso.

2.2 SIMIND: Monte Carlo Simulation

SIMIND[47] was selected as the simulation platform for this study. It is a validated simulation platform that utilizes Monte Carlo Simulation. SIMIND allows the user to simulate photon emissions through Monte Carlo simulation with possible reconstruction [48]. The adenoma is simulated as a uniform sphere with an offset 1.5cm from the center situated on the upper central portion of the cylinder. The sphere was sized around a radius of 0.3 cm. Many parameters that are used during a SPECT imaging such as Energy window, collimator type, etc., can be changed within SIMIND. This allows a comprehensive study of how the image quality behaves concerning acquisition parameters. It is used by [40] to simulate a single photon emission as well as being used in quantitative studies [49, 50, 51].

SIMIND allows users to control the imaging parameters-camera, phantom, and activity, through a program called Change. Change allows the user to change these parameters freely while also giving the option to enter custom parameters such as phantom, activity source, and energy window to be inserted independently through the input commands. The main page of the change program can be seen in Figure 2.2, while the rest of the parameters can be found in Appendix section A.

The software CASToR [52] was used for the reconstruction of the images created by

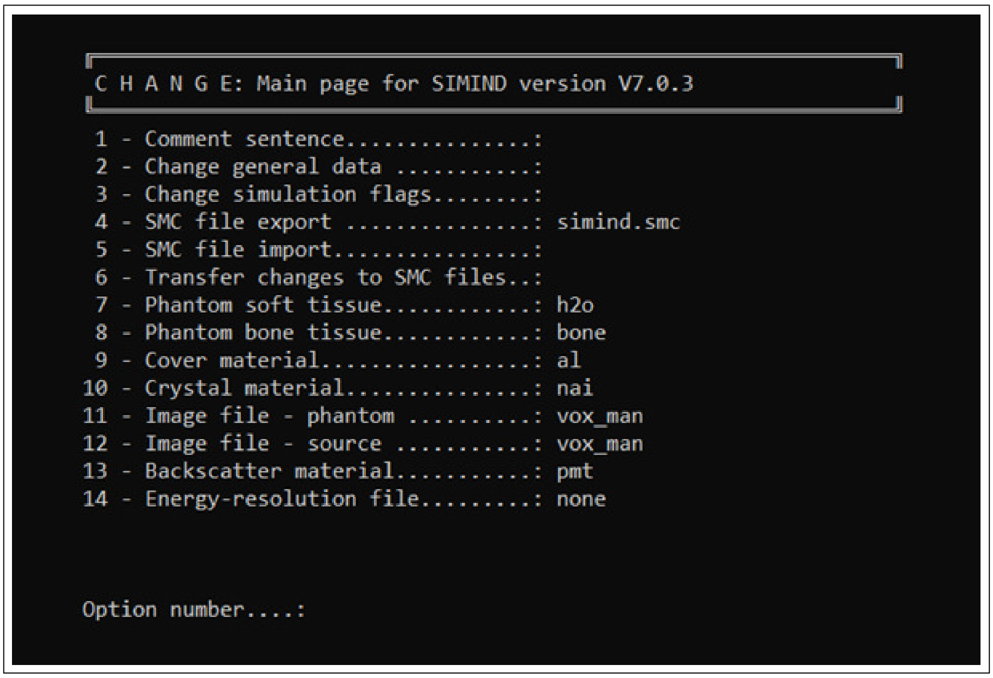

```
C H A N G E: Main page for SIMIND version V7.0.3

 1 - Comment sentence..............:
 2 - Change general data ...........:
 3 - Change simulation flags........:
 4 - SMC file export ...............: simind.smc
 5 - SMC file import................:
 6 - Transfer changes to SMC files..:
 7 - Phantom soft tissue...........: h2o
 8 - Phantom bone tissue...........: bone
 9 - Cover material.................: al
10 - Crystal material..............: nai
11 - Image file - phantom ..........: vox_man
12 - Image file - source ...........: vox_man
13 - Backscatter material...........: pmt
14 - Energy-resolution file.........: none



Option number....:
```

Figure 2.2 The main menu within change. The options to change camera materials and further parameter data can be seen. The entirety of the data will be present in Appendix A.

SIMIND simulation, CASToR is an open-source project created for the iterative reconstruction of emission (SPECT, PET) data. Using OSEM algorithms we can use differing number of iterations. In this study 16 and 32 iterations were used with 8 subsets. Since an increase in iteration number can also cause an increase in noise, we can assume that there is an iteration number that provides a balance between maximum detail and minimum noise increase.

We chose three parameters to be tested for their impact on quantification error in hyperparathyroid imaging: Collimator model (Low Energy-Ultra High Resolution, Low Energy-High Resolution), iteration number (16, 32), and presence of scatter correction. The combination sets of these parameters are given in Table 2.3.

2.3 Attenuation Correction

All SPECT images suffer from attenuation artifacts due to the effect of varying attenuation values of the object between the source and the detector surface. These

Table 2.3
The simulation/reconstruction process parameters that are being tested in regards to their effect on quantification accuracy. With parameter Scatter Correction given binary coding. (0-not used,1-used).

Collimator	Iteration	Scatter Corr.
siemens-leuhr	16	0
siemens-leuhr	16	1
siemens-leuhr	32	0
siemens-leuhr	32	1
siemens-lehr	16	0
siemens-lehr	16	1
siemens-lehr	32	0
siemens-lehr	32	1

artifacts affect the quantification of the images and applying methods to correct this effect is a must. To correct this effect, the attenuation coefficients of the object in question need to be known during the reconstruction stage of the image [7]. With the advent of SPECT/CT which allows the acquisition of both imaging modalities for the patient with presumably shared positional information, gathering attenuation maps has become much more available [34]. During reconstruction, CASToR can perform attenuation correction. Attenuation correction has been featured in all images within this study.

2.4 Scatter Correction

One of the many factors that affect SPECT imaging is Compton photon scattering. Among the many methods to correct this effect is the Triple-Energy-Window (TEW) method proposed by Koichi Ogawa is one of the simplest [37, 53]. According to this method, the scattering effect on a certain energy window could be corrected by subtraction of the counts examined in the two neighboring energy windows as given in [53]. This technique allows us to administer scatter correction after the reconstruction, thus giving us a chance to compare it against its non-scatter corrected counterpart.

We used three energy windows with the primary photopeak at 140 keV [4]. These energy windows and their respective width can be found in Table 2.4, in addition to the collective spectra of the images in Figure 2.3.

Table 2.4

Energy windows utilized in the study. With the central window 133-147 keV and the two neighboring energy windows used in the scatter correction process. The window-with represents the distance between the 140 keV mark and the upper and lower limits of the windows.

Window	Window Limits(keV)	Window Width
1	133-147	10%
2	147-168	15%
3	112-133	15%

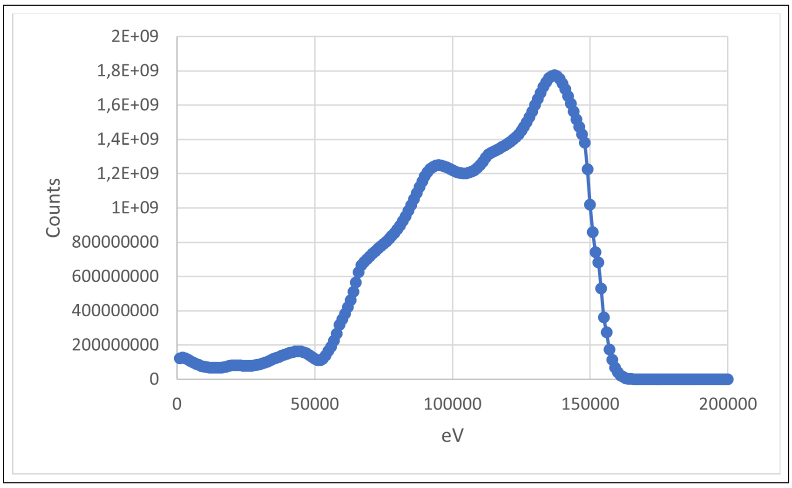

Figure 2.3 The energy Spectra of the Siemens Symbia Intevo Gamma Camera for LEUHR Collimator, where we can see the triple energy window centered around 140 keV main window and every dot representing an event.

2.5 Calibration

In the field of nuclear medicine, there is a significant need for the standardization of dosimetry and characterization of the imaging system. Since there is an abundance of factors that could influence the resulting counts in the output, calibration of the system is crucial for quantitative imaging [54, 22, 55, 43]. This study used a previously validated image-based calibration protocol [54]. This calibration method by A. Halty [54] uses the count numbers in each pixel to create an image-based calibration factor

S_{std}. The calibration factor for each image was found by calibrating the number of counts found in the images to the known input radioactivity. System calibration factor S_{tot} was found by pooling the individual calibration factors gathered from each image.

$$S_{std} = \frac{N_{SPECT}}{A_{mean} \times \Delta T_{acq}} \tag{2.1}$$

[54] suggests using the Eq. 2.1 to calculate the individual calibration factor Sstd. We slightly modified this equation to calibrate our images on a Bq/cc basis. Which might offer a better insight regarding adenomas that are not uniform.

$$S_{std} = \frac{N_{Bq/cc}}{A_{mean} \times \Delta T_{acq}} \tag{2.2}$$

$$N_{Bq/cc} = \frac{N_{SPECT}}{N_{Voxel} \times 76.62} \tag{2.3}$$

$N_{Bq/cc}$: The number of counts per cc in the adenoma. The adenoma should be segmented before this measurement is made (as given in the Segmentation chapter).
N_{voxel}: The number of voxel that adenoma spans. This value along with the NBq/cc could be found by using quantitative reporting and segmentation algorithms. This value is multiplied by 76.62 to reflect the voxel to cc change in Eq. 2.3 .
A_{mean}: Mean activity over the acquisition duration ΔT_{acq}.
ΔT_{acq}: The acquisition duration of the image. (33s for this study)
Using the Eq. 2.2 we can find individual calibration factors for every image. We choose to pool these factors to get a cohesive understanding of the system and gather a singular pooled calibration factor S_{tot}. We discovered that for better accuracy all image types should be counted in this average, such as images with and without scatter correction, lower and higher iteration, and other image-altering settings.

$$S_{tot} = \frac{\sum_{i=0}^{n} S_{std_i}}{n} \tag{2.4}$$

n: The number of images that are being pooled.
One thing to keep in mind with this method is to make sure that the same iteration numbers are counted when dealing with components such as scatter correction. This means for example if one uses iteration number a with scatter correction, they should also use iteration number a without scatter correction.

2.6 Segmentation

For the analysis and segmentation of the radioactive sphere placed within the phantom 3D-Slicer was used [56]. Using various plugins such as quantitative reporting and radiomics, we were able to observe: the mean radioactivity per voxel, the voxel-wise size of the adenoma, the coordinates of the adenoma center, etc. For segmentation, an auto segmentation algorithm, the OTSU 3D Segmentation algorithm was used [57, 58, 59, 60]. Otsu is a popular non-parametric method in image segmentation and has precedent in the use of medical imaging [59].

Radiomics is a discipline that uses automated algorithms to improve the quantification of phenotypic characterizations in medical imaging. These algorithms -whether hard coded or deep learning-based can be used to develop non-invasive imaging-based biomarkers. Within the 3D Slicer program, these algorithms are available as the Radiomics extension [61]. In this study, the Radiomics extension is utilized in tandem with the Quantitative Reporting extension [62]. The selection to use an auto-segmentation algorithm was made to eliminate the human factor in segmentation, in favor of mathematical algorithms for the most objective segmentation and quantification accuracy. The results of segmentation are given in Figure 2.4, where the thresholding done by the OTSU algorithm can be seen.

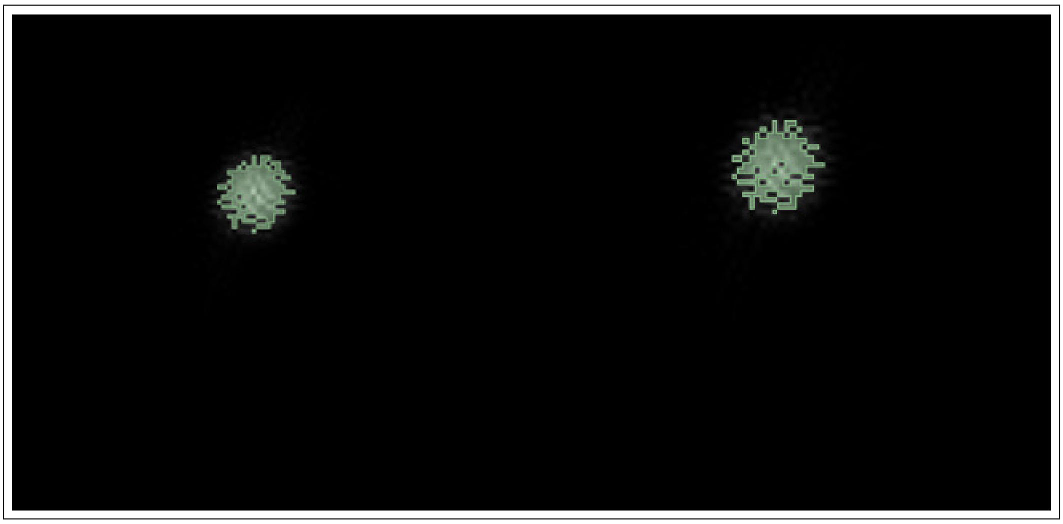

Figure 2.4 Examples of Siemens Symbia Gamma camera image output volumes segmented by the OTSU 3D algorithm in transaxial view using LEUHR(left) and LEHR(right) collimators, with a spherical source.

2.7 Error Analysis

Quantification errors are identified by performing a straightforward quantitative analysis [63] that compares the simulated radioactivity value ($N_{simulated}$) as provided in the Simind output page with the radioactivity value observed within the segmented adenoma section ($N_{observed}$). You can locate the Simind output values in Sections 3.1 and 3.2. Meanwhile, the observed value is determined using the 3D-Slicer program and radiomics. The equation for this analysis is presented below(Eq. 2.5).

$$ErrorPercentage = \frac{N_{simulated} - N_{observed}}{N_{Simulated}} x100 \tag{2.5}$$

3. RESULTS

The results (Tables 3.1 and 3.2) show that the change of parameters can result in a nearly 20% relative change in quantification error. The quantification error for the scatter-corrected images was found around %10 or below. When low energy-ultra high-resolution collimator was used with scatter correction and 32 iterations the error was found to be as low as 7%. The quantification error for the simulated images was found around 9 percent or below which is in line with the desired results of a sub-10 percent error.

3.1 Siemens Low-Energy Ultra High-Resolution Collimator Results

```
        SIMIND Monte Carlo Simulation Program V7.0.3
------------------------------------------------------------------
Phantom(S): h2o      Crystal...: nai      InputFile.: cylinder
Phantom(B): bone      BackScatt.: pmt      OutputFile: cylinder
Collimator: pb_sb2      SourceRout : jaszak      SourceFile : none
Cover..... : al      ScoreRout. : scattwin      DensityMap : none
------------------------------------------------------------------
PhotonEnergy.......: 140                tc99m PhotonsPerProj....: 5000000
EnergyResolution...: 10                 sy-leuh Activity..........: 13629
MaxScatterOrder....: 3                  SPECT DetectorLenght....: 29.55
DetectorWidth......: 22                 Random DetectorHeight....: 0.95
UpperEneWindowTresh: 154                     Phantom Distance to det...: 31
LowerEneWindowTresh: 126                     Resolut ShiftSource X.....: 0
PixelSize I.......: 0.24              Header ShiftSource Y.....: 0
PixelSize J.......: 0.24              ShiftSource Z.....: 0
HalfLength S.......: 0.38               HalfLength P......: 30
HalfWidth S.......: 0.38                HalfWidth P......: 11
```

```
HalfHeight S.......: 0.38          HalfHeight P......: 11
SourceType.........: MultiSphere          PhantomType.......: VerCylinder
```

```
    GENERAL DATA
keV/channel........: 512          CutoffEnergy......: 0
Photons/Bq.........: 0.89821          StartingAngle.....: 0
CameraOffset X.....: 0          CoverThickness....: 0
CameraOffset Y.....: 0          BackscatterThickn.: 0
MatrixSize I.......: 128          IntrinsicResolut..: 0.36
MatrixSize J.......: 128          AcceptanceAngle...: 2.74319
Emission type......: 2          Initial Weight....: 2448.34475
NN ScalingFactor...: 1          Energy Channels...: 512
```

```
SPECT DATA
RotationMode.......: 180          Nr of Projections.: 48
RotationAngle......: 3.75          Projection.[start]: 1
Orbital fraction...: 1          Projection...[end]: 48
```

```
COLLIMATOR DATA FOR ROUTINE: Analytical
CollimatorCode.....: sy-leuh          CollimatorType....: Parallel
HoleSize X.........: 0.15          Distance X........: 0.02
HoleSize Y.........: 0.17321          Distance Y........: 0.10392
CenterShift X......: 0.085          X-Ray flag........: F
CenterShift Y......: 0.14722          CollimThickness...: 3.5
HoleShape..........: Hexagonal          Space Coll2Det....: 0
CollDepValue [57]..: 0          CollDepValue [58].: 0
CollDepValue [59]..: 0          CollDepValue [60].: 0
```

```
MULTIPLE SOURCE CONFIGURATION
```

```
Source    Volume(ml)    MBq     kBq/ml      Shape
1         14.1372       13629   964.0545    Ellipsoid
```

```
Photon energy      Abundance
20.669 keV        0.1120E-01
21.023 keV        0.1770E-02
89.600 keV        0.1040E-04
140.511 keV        0.8850
142.683 keV        0.2300E-03
232.700 keV        0.8400E-07
322.400 keV        0.9600E-06
```

```
Scattwin results: Window file: jaszak.win
Win    WinAdded    Range(keV)     ScaleFactor
1          0       133.0 - 147.0   1.00
2          0       147.0 - 168.0   0.33
3          0       112.0 - 133.0   0.33
Win   Total     Scatter    Primary   S/P-Ratio   S/T Ratio   Cps/MBq
1  0.108E+08  0.296E+07  0.781E+07  0.379E+00  0.275E+00  0.165E+02
2  0.160E+07  0.177E+06  0.143E+07  0.124E+00  0.110E+00  0.245E+01
3  0.104E+08  0.789E+07  0.250E+07   0.315E+01  0.759E+00  0.159E+02
Win  Geo(Air)  Pen(Air)  Sca(Air)  Geo(Tot)  Pen(Tot)  Sca(Tot)
1  100.00%  0.00  0.00  100.00%  0.00  0.00
2  100.00%  0.00  0.00  100.00%  0.00  0.00
3  100.00%  0.00  0.00  100.00%  0.00  0.00
Win   SC 1   SC 2   SC 3
1     87.4%  11.5%  1.0%
2     94.3%  5.5%  0.3%
3     64.3%  28.9%  6.8%
```

INTERACTIONS IN THE CRYSTAL

MaxValue spectrum..: 7.390

MaxValue projection: 5581.

CountRate spectrum.: 0.1540

CountRate E-Window.: 0.3296E+06

PHOTONS AFTER COLLIMATOR AND WITHIN ENER-WIN

Geometric..........: 0.00 % 100.00 %

Penetration........: 0.00 % 0.00 %

Scatter in collim..: 0.00 % 0.00 %

X-rays in collim...: 0.00 % 0.00 %

SCATTER IN ENERGY WINDOW

Scatter/Primary....: 0.56457

Scatter/Total......: 0.36085

Scatter order 1....: 82.41 %

Scatter order 2....: 15.65 %

Scatter order 3....: 1.94 %

CALCULATED DETECTOR PARAMETERS

Efficiency E-Window: 0.4013

Efficiency spectrum: 0

Sensitivity Cps/MBq: 24.1827

Sensitivity Cpm/uCi: 53.6857

Simulation started.: 2023:05:04 15:20:50

Simulation stopped.: 2023:05:04 15:32:47

Elapsed time.......: 0 h, 11 m and 57 s

DetectorHits.......: 18613498

DetectorHits/CPUsec: 26002

SIMIND built 2022:11:25 with INTEL Win compiler

Random number generator: ranmar

Comment:EMISSION

Energy resolution as function of 1/sqrt(E)

Table 3.1
Quantification accuracy results of Siemens Symbia Intevo Gamma Camera Using LEUHR collimator.

	Parameters		Quantification Error
Collimator	Iteration	Scatter Corr	MBq/cc
siemens-leuhr	16	0	7.5%
siemens-leuhr	16	1	7%
siemens-leuhr	32	0	7.3%
siemens-leuhr	32	1	7.1 %

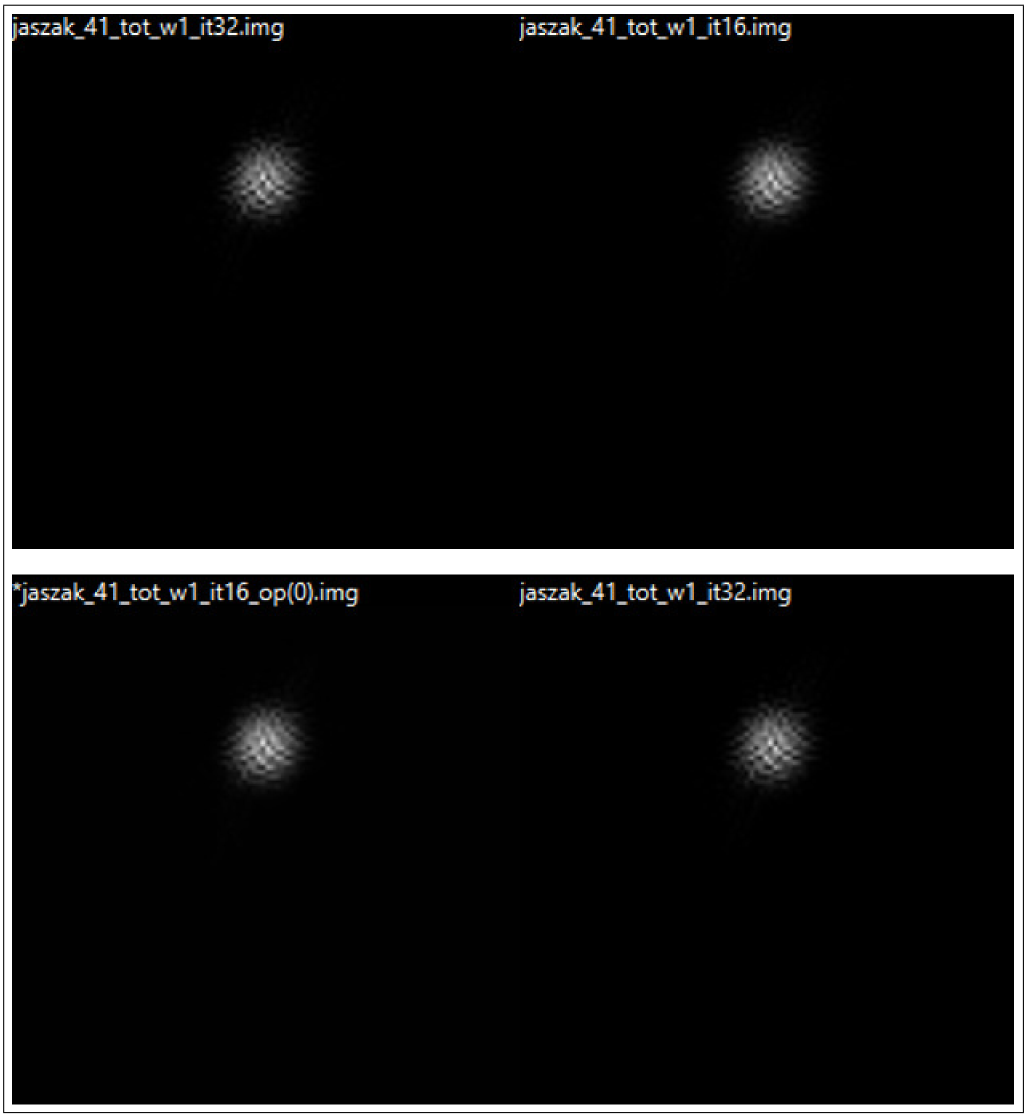

Figure 3.1 The resulting images from reconstruction with 32 iterations and no scatter correction(top-left), 16 iterations and no scatter correction(top-right), 16 iterations and scatter correction(bottom-left), 32 iterations and scatter correction(bottom-right).

3.2 Siemens Low-Energy High-Resolution Collimator Results

SIMIND Monte Carlo Simulation Program V7.0.3

Phantom(S): h2o Crystal...: nai InputFile.: cylinder

Phantom(B): bone BackScatt.: pmt OutputFile: cylinder

Collimator: pb$_sb2$ $SourceRout : jaszak$ $SourceFile : none$

```
Cover..... : al        ScoreRout. : scattwin        DensityMap : none
---------------------------------------------------------------------------

PhotonEnergy.......: 140              tc99m PhotonsPerProj....: 5000000
EnergyResolution...: 10               sy-leuh Activity..........: 13629
MaxScatterOrder....: 3               SPECT DetectorLenght....: 29.55
DetectorWidth......: 22              Random DetectorHeight....: 0.95
UpperEneWindowTresh: 154                  Phantom Distance to det...: 31
LowerEneWindowTresh: 126                  Resolut ShiftSource X.....: 0
PixelSize I.......: 0.24            Header ShiftSource Y.....: 0
PixelSize J.......: 0.24            ShiftSource Z.....: 0
HalfLength S.......: 0.38             HalfLength P......: 30
HalfWidth S.......: 0.38             HalfWidth P......: 11
HalfHeight S.......: 0.38             HalfHeight P......: 11
SourceType.........: MultiSphere            PhantomType.......: VerCylinder

---------------------------------------------------------------------------


     GENERAL DATA
keV/channel........: 512             CutoffEnergy......: 0
Photons/Bq.........: 0.89821             StartingAngle.....: 0
CameraOffset X.....: 0              CoverThickness....: 0
CameraOffset Y.....: 0              BackscatterThickn.: 0
MatrixSize I.......: 128             IntrinsicResolut..: 0.36
MatrixSize J.......: 128             AcceptanceAngle...: 2.74319
Emission type......: 2              Initial Weight....: 2448.34475
NN ScalingFactor...: 1              Energy Channels...: 512
---------------------------------------------------------------------------

SPECT DATA
RotationMode.......: 180              Nr of Projections.: 48
RotationAngle......: 3.75              Projection.[start]: 1
Orbital fraction...: 1             Projection...[end]: 48

---------------------------------------------------------------------------
```

```
COLLIMATOR DATA FOR ROUTINE: Analytical
CollimatorCode.....: sy-lehr        CollimatorType....: Parallel
HoleSize X.........: 0.111          Distance X........: 0.016
HoleSize Y.........: 0.12817        Distance Y........: 0.07794
CenterShift X......: 0.10999        X-Ray flag........: F
CenterShift Y......: 0.0635         CollimThickness...: 2.405
HoleShape..........: Hexagonal      Space Coll2Det....: 0
CollDepValue [57]..: 0              CollDepValue [58].: 0
CollDepValue [59]..: 0              CollDepValue [60].: 0
```

```
MULTIPLE SOURCE CONFIGURATION
Source   Volume(ml)   MBq     kBq/ml     Shape
1        14.1372      13629   964.0545   Ellipsoid
```

```
Photon energy      Abundance
20.669 keV       0.1120E-01
21.023 keV       0.1770E-02
89.600 keV       0.1040E-04
140.511 keV        0.8850
142.683 keV        0.2300E-03
232.700 keV        0.8400E-07
322.400 keV        0.9600E-06
```

```
Scattwin results: Window file: jaszak.win
Win   WinAdded   Range(keV)      ScaleFactor
1        0       133.0 - 147.0   1.00
2        0       147.0 - 168.0   0.33
3        0       112.0 - 133.0   0.33
Win   Total     Scatter    Primary    S/P-Ratio  S/T Ratio  Cps/MBq
1  0.133E+08  0.361E+07  0.965E+07  0.374E+00  0.272E+00  0.203E+02
```

```
2   0.198E+07  0.217E+06  0.176E+07  0.123E+00  0.110E+00  0.303E+01
3   0.126E+08  0.974E+07  0.310E+07   0.305E+01  0.753E+00  0.192E+02
Win   Geo(Air)  Pen(Air)  Sca(Air)   Geo(Tot)   Pen(Tot)   Sca(Tot)
1   93.70%   4.81   1.49  93.85%   4.69   1.45
2   93.80%   4.80   1.40   93.84%   4.76   1.40
3   93.34%   4.77   1.89   94.75%   3.80   1.45
Win     SC 1    SC 2    SC 3
1         87.9%  11.1%   1.0%
2         94.5%  5.3%   0.2%
3         64.9%  28.6%   6.5%
```

```
INTERACTIONS IN THE CRYSTAL
MaxValue spectrum..: 7.390
MaxValue projection: 5581.
CountRate spectrum.: 0.1540
CountRate E-Window.: 0.3296E+06
```

```
PHOTONS AFTER COLLIMATOR AND WITHIN ENER-WIN
Geometric..........:    94.53 %      93.59 %
Penetration........:    3.69 %      4.58 %
Scatter in collim..:    1.78 %      1.47 %
X-rays in collim...:    0.00 %      0.00 %
```

```
SCATTER IN ENERGY WINDOW
Scatter/Primary....: 0.5553
Scatter/Total......: 0.35704
Scatter order 1....: 82.96 %
Scatter order 2....: 15.22 %
Scatter order 3....: 1.82 %
```

```
CALCULATED DETECTOR PARAMETERS
Efficiency E-Window: 0.4044
Efficiency spectrum: 0
Sensitivity Cps/MBq: 29.6977
Sensitivity Cpm/uCi: 65.929
```

```
Simulation started.: 2023:05:09 16:05:46
Simulation stopped.: 2023:05:09 17:11:34
Elapsed time.......: 1 h, 5 m and 48 s
DetectorHits.......: 6028184
DetectorHits/CPUsec: 1826
```

```
SIMIND built 2022:11:25 with INTEL Win compiler
Random number generator: ranmar
Comment:EMISSION
Energy resolution as function of 1/sqrt(E)
```

Table 3.2
Quantification accuracy results of Siemens Symbia Intevo Gamma Camera Using LEHR collimator.

	Parameters		Quantification Error
Collimator	Iteration	Scatter Corr	MBq/cc
siemens-lehr	16	0	8.3%
siemens-lehr	16	1	7.6%
siemens-lehr	32	0	8.5%
siemens-lehr	32	1	8.7 %

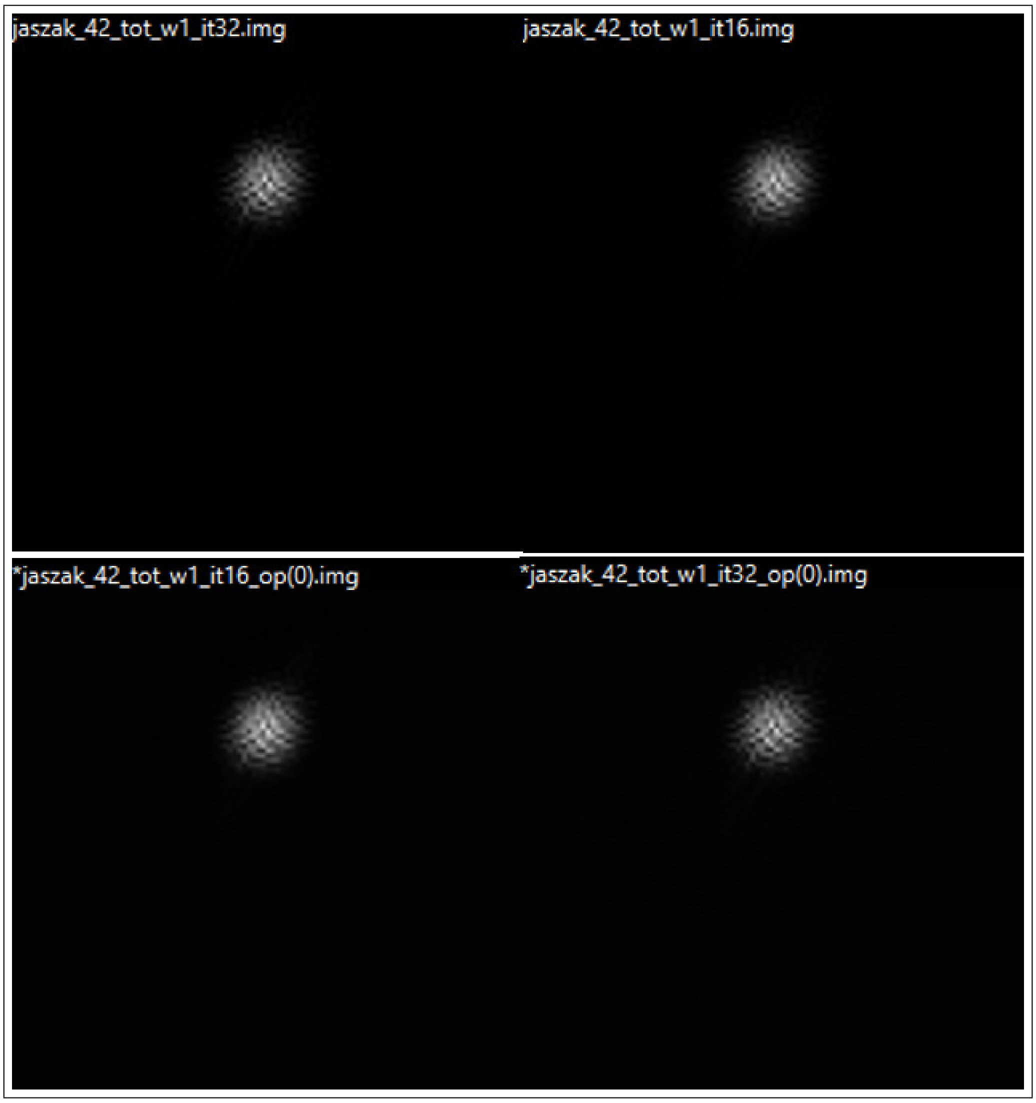

Figure 3.2 The resulting images from reconstruction with 32 iterations and no scatter correction(top-right), 16 iterations and no scatter correction(top-left), 16 iterations and scatter correction(bottom-left), 32 iterations and scatter correction(bottom-right).

4. DISCUSSION

This study aimed to simulate and observe the effects of differing simulation and processing parameters on the quantification accuracy of hyperactive parathyroid glands using Tc-99m MIBI dual-phase parathyroid SPECT/CT.

According to [64], the presence of attenuation and scatter correction can cause a 25 percent difference in the observed radioactivity level in water-filled phantoms which is consistent relative with our results. We observed a consistent improvement in accuracy when scatter correction was applied to experiments. While the absence of both is stated to cause a nearly 50 percent error rate [64], we see this as a plausible possibility. [65] reports that using commercial tools a quantification accuracy of 1-4 percent can be achieved. This is consistent also with our observations of around 7 percent possible accuracy improvement made with open-source programs such as SIMIND and CASToR.

This study is exercised with three different simulation and process parameters: the collimator, iterative reconstruction number, and the presence of scatter correction. During the simulation, a uniform adenoma within a digital cylindrical phantom filled with water was used. These experiments with rather simple parameter sets were selected to showcase the quantification capabilities of SPECT imaging and can become a basis for any further studies looking to experiment with other parameters as well as more complicated phantoms and reconstruction algorithms.

An anthropomorphic phantom could be used within this study to further examine situations resembling real life. The current cylindrical phantom provides advantages in having uniform density and low background activity which makes it easier to segment the adenoma. However, its lack of biological structures and attenuation is another limitation of this study.

The number of iterations has also been observed to be effective in improving accuracy. This is reasonable considering the optimization-based reconstruction algorithms (MLEM) used. However, higher iterations also certainly mean higher process times and delayed outputs. So, the users should be encouraged to keep a balanced approach when tackling this issue. Also, the processing power of the system is seen as highly affecting the processing time, so this should also be in consideration.

The type of collimator makes a difference. We observed that the higher resolution LEUHR collimator results in higher accuracy than LEHR. We observed an accuracy difference of around 1-1.5% percent in relative comparison between these types of collimators. The collimators have shown a consistent difference in error rate with LEUHR having a quantification error of lower 7 percent while LEHR achieved an error rate of around 8.5 percent. These results give us an idea about the effect septal properties(Table 2.2) have on quantitative accuracy with both collimators operating on low energy.

Scatter correction was seen to influence the results, by 1-1.5 percent in certain instances. When put into perspective, this is around a 15 percent improvement relative to the accuracy without scatter correction. This puts forward the capabilities and importance of this correction method as scattering is a factor present in every imaging modality where photon radiation is present. In further studies, the importance of scatter correction might be increased with biological structures all having different attenuation coefficients. Additionally, within the open-source programs SIMIND and CASToR, it is not possible to employ resolution recovery, dead time correction, and partial volume correction which is another limitation in our study. In the end, we can say with confidence, the results show that parameters used in imaging have a considerable impact on the quantification accuracy.

5. CONCLUSION

This study undertakes for the first time the optimization of quantitative parathyroid SPECT by the use of computer simulation and we believe this study will advance the use of this technique. However, more clinical studies are needed.

Quantification is shown to be a method that holds immense potential for the future of medical imaging. It gives the user the ability to identify and characterize an adenoma in a precise and accurate manner. Within precision medicine, robustness and adaptability are essential. Thus, making the study of different parameters and their effects on quantification a must.

In this study, we have concluded that simulation and processing parameters have observable effects on quantification accuracy. In Figure 3, it can be seen that the presence of scatter correction, the number of iterations, and the collimators have differing effects on quantification accuracy. However, all parameter sets have achieved a sub-10 percent quantification accuracy. Thus, we show the viability of SPECT as a quantitative imaging modality.

We conclude within this study that quantitative imaging is a field that could be improved upon and is open to a very wide array of possibilities as far as newer studies. The role quantitative imaging plays in precise medicine puts this technique at the forefront of medical innovation. Especially during challenging procedures like parathyroid imaging, where placement and size of the subject in question make imaging very difficult. In this field accuracy and precision are paramount in reducing error and invasiveness in treatment and quantitative imaging just might give the health professionals the needed edge.

5.1 Limitations

When performing quantification, it is paramount to gather an accurate representation of the voxel-vise volume of the edges of the object. This puts a lot of attention on the segmentation of the adenoma. During this study, we used sources with similar attributes. However, as the adenoma size varies and gets smaller, the ability to accurately segmentate this adenoma gets harder. Under these circumstances, it could be hard to find a one-size-fits-all solution to the segmentation problem. This situation has proven to be a limitation of the study.

In a published study, [66] has found that quantitative analysis could be used to characterize parathyroid lesions such as carcinomas, adenomas, and hyperplasia. This study was done on the adenoma lesion type. Thus, for accurate optimization of differing lesion types, experiments involving those lesion types should be made.

5.2 Future Works

Within this study, a base set of parameters was used to examine the differences in quantitative accuracy. In further studies, these parameters can be built upon closer to real-life situations.

During the study two low-energy collimators with differing resolution and septal properties (LEHR and LEUHR) were used. In addition to these two collimator models, low-energy all-purpose (LEAP) and low-energy fan beam (LEFB) models could be used to further demonstrate the effect of collimators on quantification accuracy.

Resolution recovery is a correction method used to reduce the necessary dose needed for imaging during the reconstruction process. It is only available alongside iterative reconstruction. Images created by resolution recovery provide better contrast and resolution while needing less acquisition and processing time [67]. This method should be further examined for its effect on quantification accuracy. Other correction methods such as dead time correction and partial volume correction further improve the precision of the image which is proven to be very important in quantitative studies and should also be employed in future studies.

The addition of anthropomorphic phantom types to the testing can improve our understanding of this study with closer to real-life circumstances. It also introduces further challenges such as segmentation alongside background activity and attenuation. Simulating and testing different gamma camera models would expand the spectrum this study encompasses. Since most gamma camera models have different imaging parameters, their effects could also be researched.

APPENDIX A. PARAMETERS USED DURING THE STUDY

A.1 SIMIND Monte Carlo Simulation

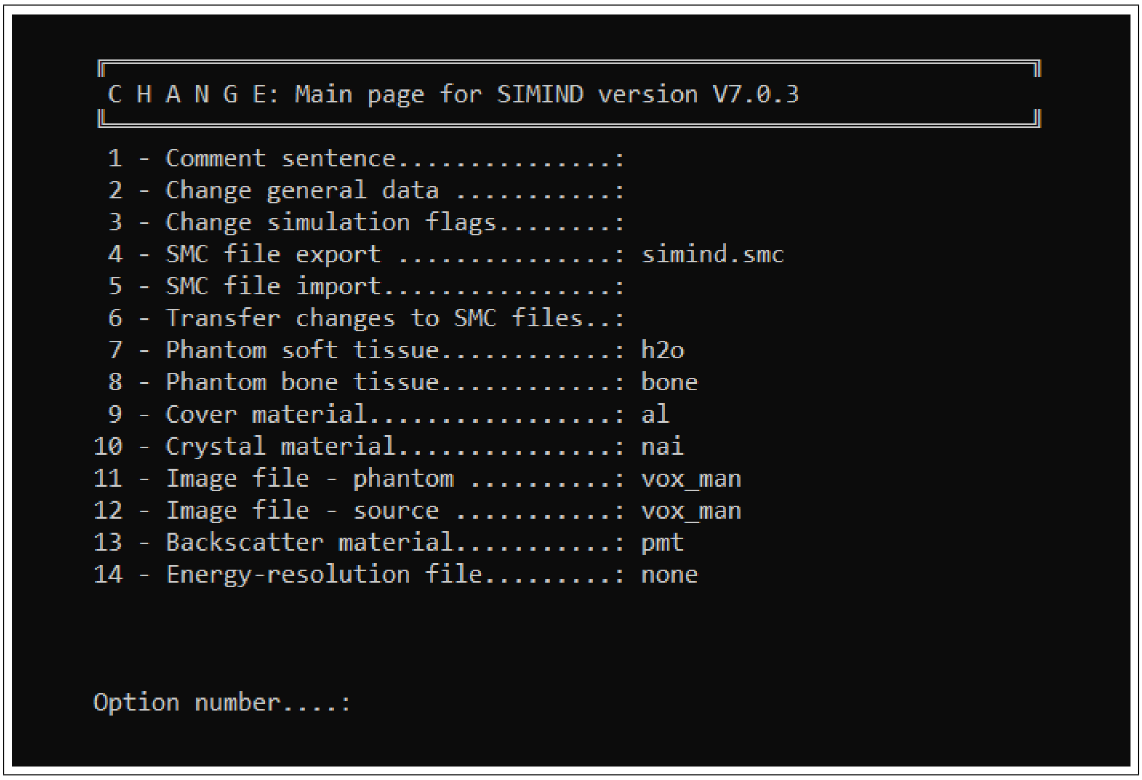

```
╔════════════════════════════════════════════════════════════════╗
 C H A N G E: Main page for SIMIND version V7.0.3
╚════════════════════════════════════════════════════════════════╝
 1 - Comment sentence...............:
 2 - Change general data ...........:
 3 - Change simulation flags........:
 4 - SMC file export ...............: simind.smc
 5 - SMC file import................:
 6 - Transfer changes to SMC files..:
 7 - Phantom soft tissue............: h2o
 8 - Phantom bone tissue............: bone
 9 - Cover material.................: al
10 - Crystal material...............: nai
11 - Image file - phantom ..........: vox_man
12 - Image file - source ...........: vox_man
13 - Backscatter material...........: pmt
14 - Energy-resolution file.........: none



Option number....:
```

Figure A.1 The main menu of the SIMIND simulation program that allows the user to navigate.

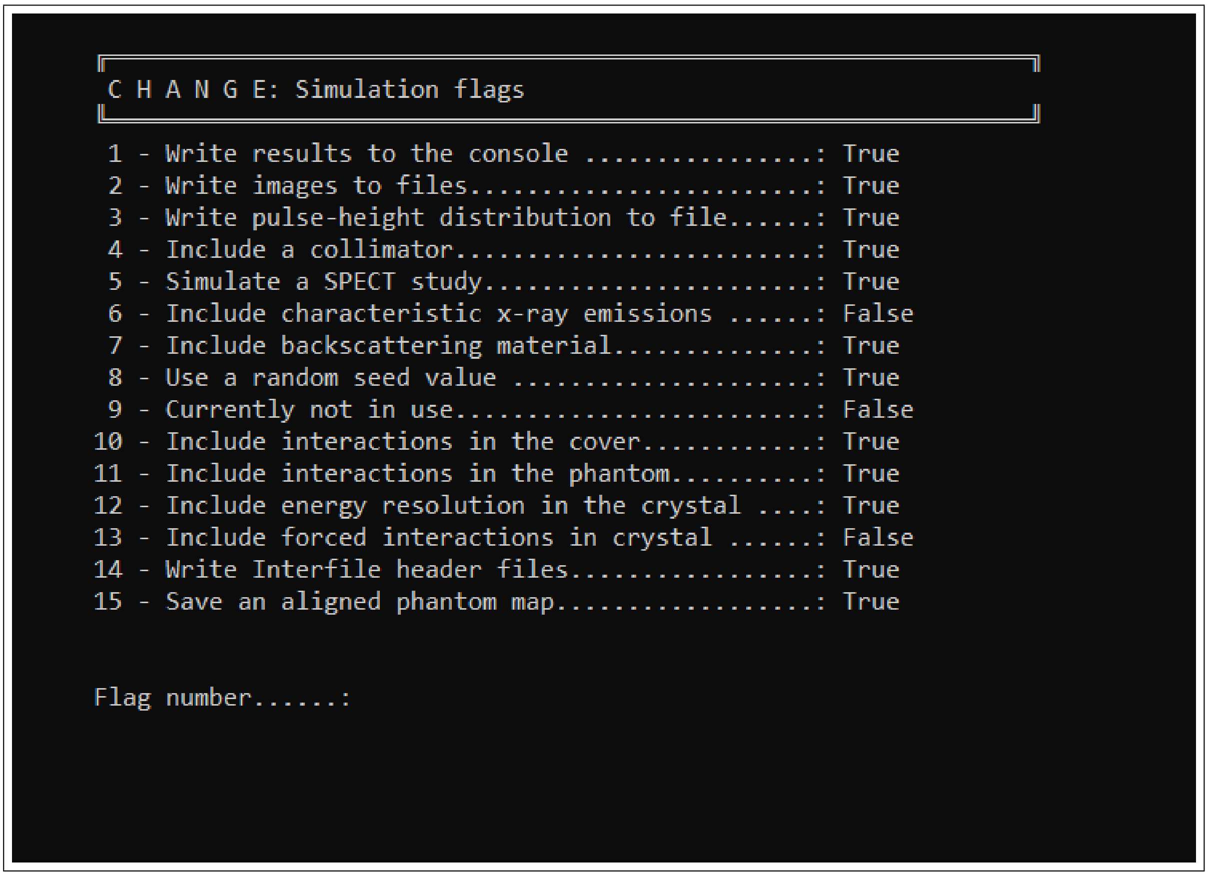

```
C H A N G E: Simulation flags

 1 - Write results to the console ................: True
 2 - Write images to files........................: True
 3 - Write pulse-height distribution to file......: True
 4 - Include a collimator.........................: True
 5 - Simulate a SPECT study.......................: True
 6 - Include characteristic x-ray emissions ......: False
 7 - Include backscattering material..............: True
 8 - Use a random seed value .....................: True
 9 - Currently not in use.........................: False
10 - Include interactions in the cover............: True
11 - Include interactions in the phantom..........: True
12 - Include energy resolution in the crystal ....: True
13 - Include forced interactions in crystal ......: False
14 - Write Interfile header files.................: True
15 - Save an aligned phantom map..................: True


Flag number......:
```

Figure A.2 Simulation flags that enable different simulation options.

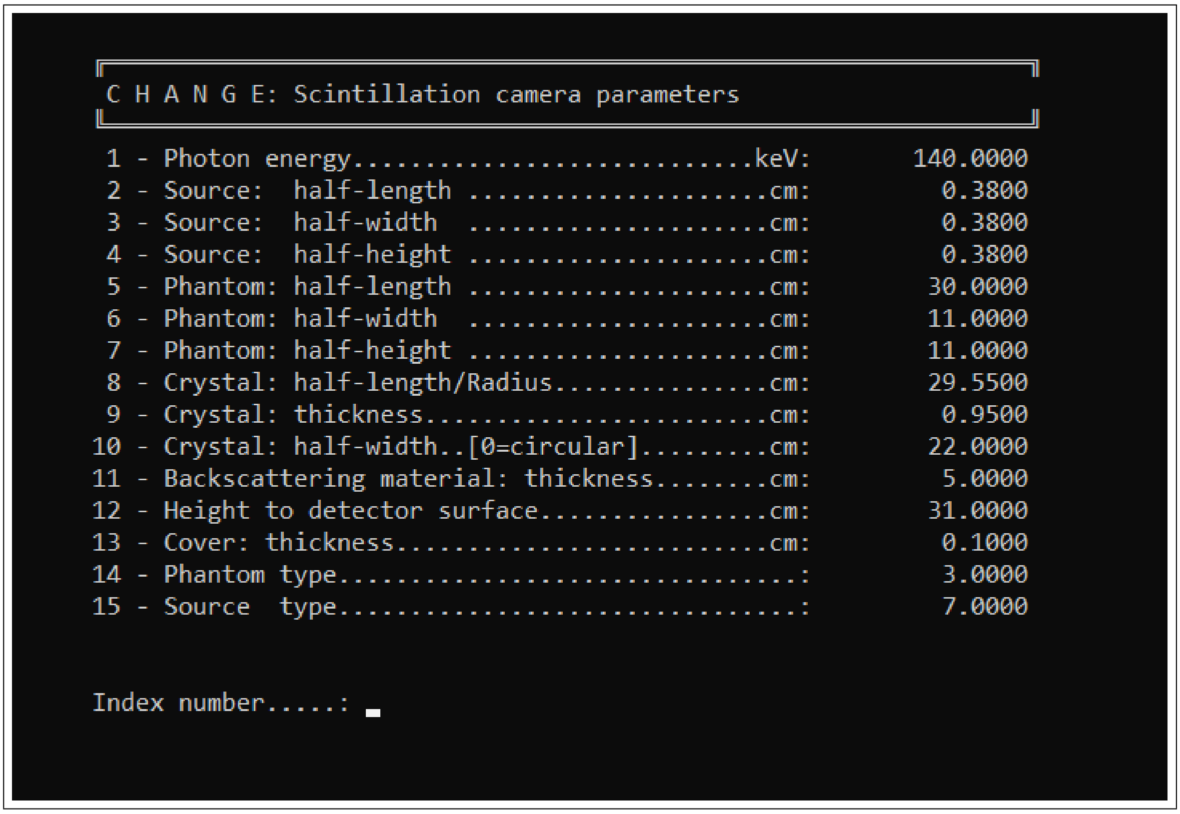

```
╔═════════════════════════════════════════════════════════════╗
 C H A N G E: Scintillation camera parameters
╚═════════════════════════════════════════════════════════════╝
 1 - Photon energy............................keV:      140.0000
 2 - Source:  half-length .....................cm:        0.3800
 3 - Source:  half-width  .....................cm:        0.3800
 4 - Source:  half-height .....................cm:        0.3800
 5 - Phantom: half-length .....................cm:       30.0000
 6 - Phantom: half-width  .....................cm:       11.0000
 7 - Phantom: half-height .....................cm:       11.0000
 8 - Crystal: half-length/Radius...............cm:       29.5500
 9 - Crystal: thickness........................cm:        0.9500
10 - Crystal: half-width..[0=circular].........cm:       22.0000
11 - Backscattering material: thickness........cm:        5.0000
12 - Height to detector surface................cm:       31.0000
13 - Cover: thickness..........................cm:        0.1000
14 - Phantom type...............................:         3.0000
15 - Source  type...............................:         7.0000


Index number.....: _
```

Figure A.3 Camera parameters that are set to Siemens Symbia Intevo Camera (Like the photon energy that is set to 140keV which is the peak energy of Tc99m.).

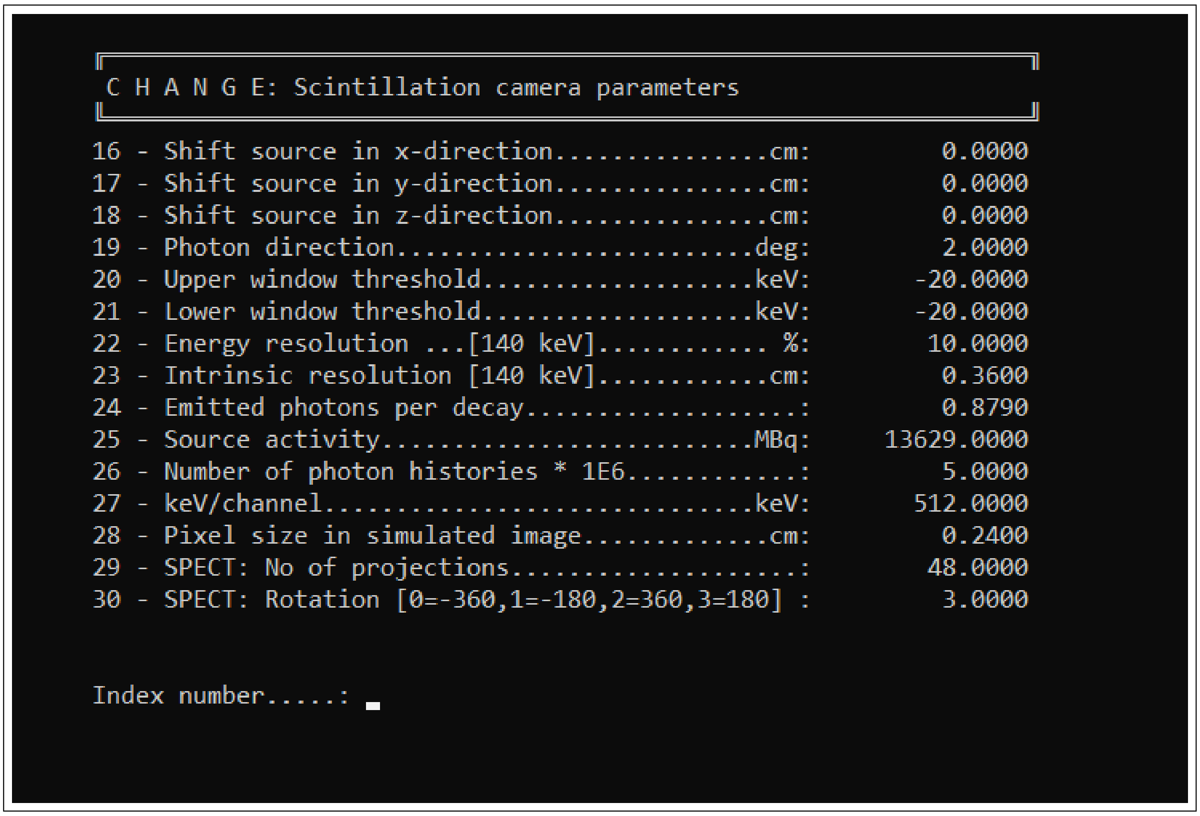

```
C H A N G E: Scintillation camera parameters

16 - Shift source in x-direction...............cm:         0.0000
17 - Shift source in y-direction...............cm:         0.0000
18 - Shift source in z-direction...............cm:         0.0000
19 - Photon direction.........................deg:         2.0000
20 - Upper window threshold...................keV:       -20.0000
21 - Lower window threshold...................keV:       -20.0000
22 - Energy resolution ...[140 keV]............ %:        10.0000
23 - Intrinsic resolution [140 keV]............cm:         0.3600
24 - Emitted photons per decay..................:         0.8790
25 - Source activity..........................MBq:     13629.0000
26 - Number of photon histories * 1E6...........:         5.0000
27 - keV/channel..............................keV:       512.0000
28 - Pixel size in simulated image............cm:         0.2400
29 - SPECT: No of projections...................:        48.0000
30 - SPECT: Rotation [0=-360,1=-180,2=360,3=180] :         3.0000


Index number.....: 
```

Figure A.4 SIMIND parameters that include energy window, source activity.

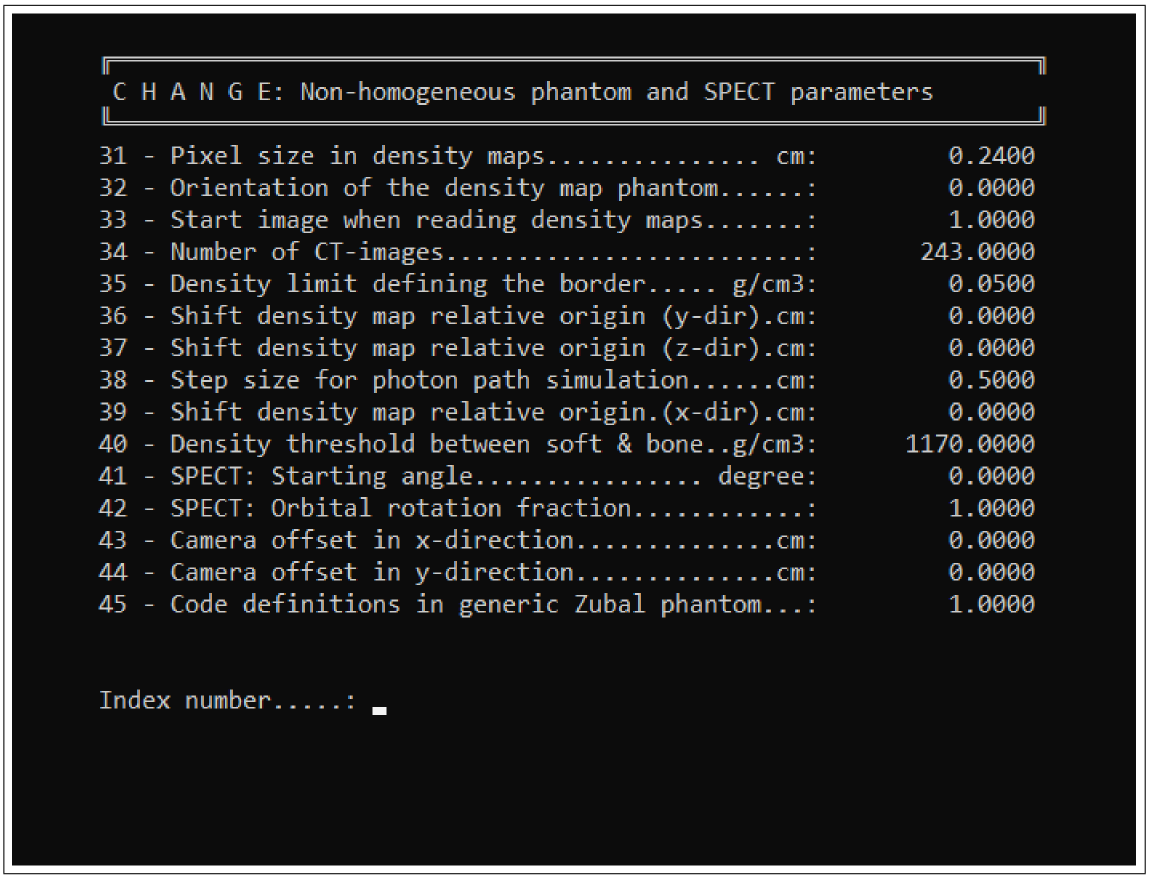

```
╔══════════════════════════════════════════════════════════════════╗
 C H A N G E: Non-homogeneous phantom and SPECT parameters
╚══════════════════════════════════════════════════════════════════╝
31 - Pixel size in density maps............... cm:         0.2400
32 - Orientation of the density map phantom......:         0.0000
33 - Start image when reading density maps.......:         1.0000
34 - Number of CT-images..........................:       243.0000
35 - Density limit defining the border..... g/cm3:         0.0500
36 - Shift density map relative origin (y-dir).cm:         0.0000
37 - Shift density map relative origin (z-dir).cm:         0.0000
38 - Step size for photon path simulation......cm:         0.5000
39 - Shift density map relative origin.(x-dir).cm:         0.0000
40 - Density threshold between soft & bone..g/cm3:      1170.0000
41 - SPECT: Starting angle................ degree:         0.0000
42 - SPECT: Orbital rotation fraction............:         1.0000
43 - Camera offset in x-direction.............cm:         0.0000
44 - Camera offset in y-direction.............cm:         0.0000
45 - Code definitions in generic Zubal phantom...:         1.0000


Index number.....: ▂
```

Figure A.5 Phantom simulation parameters that include density and positional options.

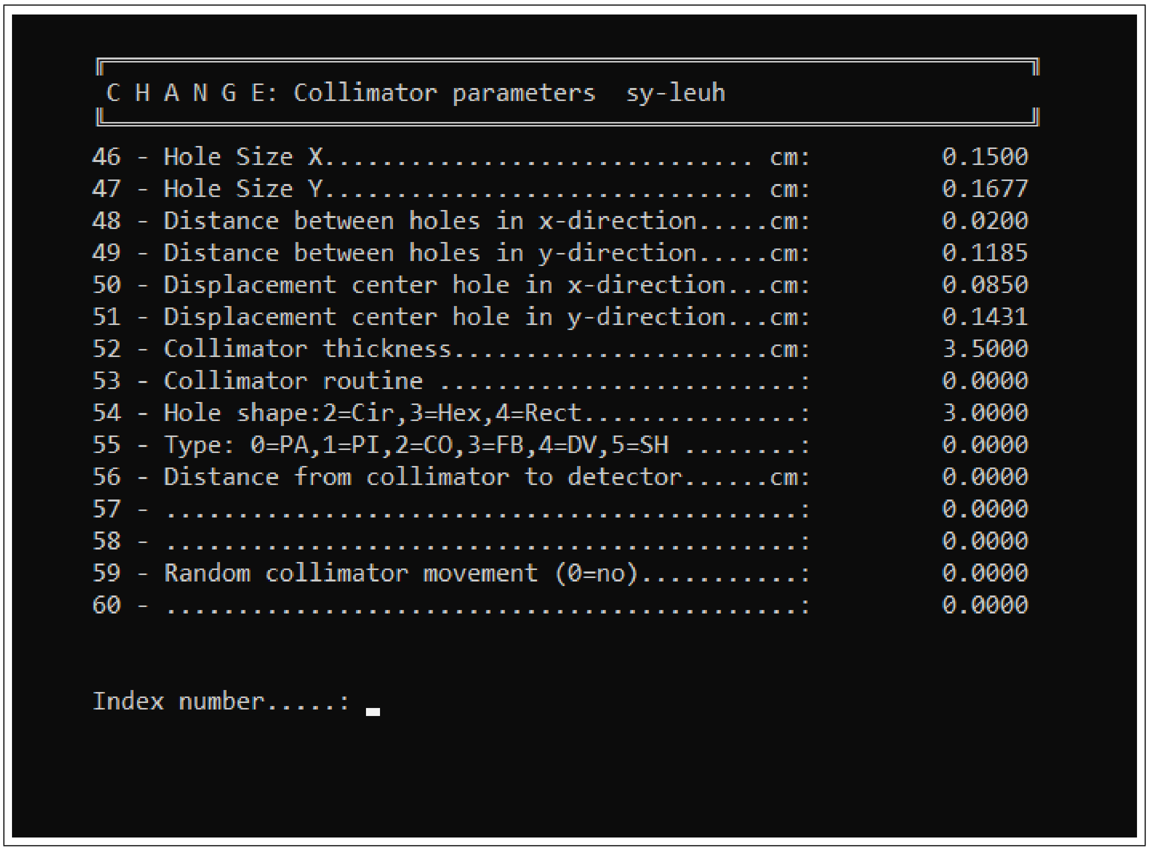

```
C H A N G E: Collimator parameters  sy-leuh

46 - Hole Size X.............................. cm:         0.1500
47 - Hole Size Y.............................. cm:         0.1677
48 - Distance between holes in x-direction.....cm:         0.0200
49 - Distance between holes in y-direction.....cm:         0.1185
50 - Displacement center hole in x-direction...cm:         0.0850
51 - Displacement center hole in y-direction...cm:         0.1431
52 - Collimator thickness......................cm:         3.5000
53 - Collimator routine .........................:         0.0000
54 - Hole shape:2=Cir,3=Hex,4=Rect................:         3.0000
55 - Type: 0=PA,1=PI,2=CO,3=FB,4=DV,5=SH ........:         0.0000
56 - Distance from collimator to detector......cm:         0.0000
57 - ............................................:         0.0000
58 - ............................................:         0.0000
59 - Random collimator movement (0=no)...........:         0.0000
60 - ............................................:         0.0000


Index number.....: _
```

Figure A.6 Collimator parameters set to Siemens LEUHR collimator.

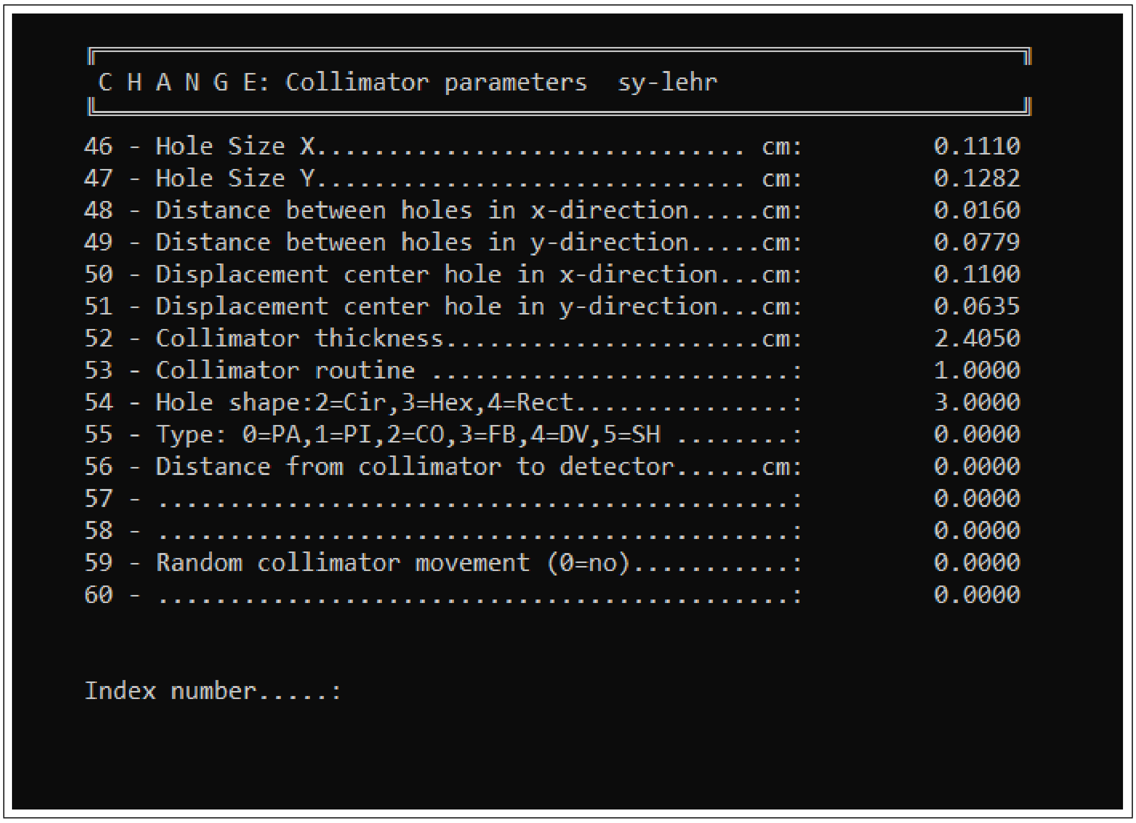

```
╓──────────────────────────────────────────────────────────────╖
 C H A N G E: Collimator parameters  sy-lehr
╙──────────────────────────────────────────────────────────────╜
46 - Hole Size X............................. cm:        0.1110
47 - Hole Size Y............................. cm:        0.1282
48 - Distance between holes in x-direction.....cm:        0.0160
49 - Distance between holes in y-direction.....cm:        0.0779
50 - Displacement center hole in x-direction...cm:        0.1100
51 - Displacement center hole in y-direction...cm:        0.0635
52 - Collimator thickness......................cm:        2.4050
53 - Collimator routine .........................:        1.0000
54 - Hole shape:2=Cir,3=Hex,4=Rect...............:        3.0000
55 - Type: 0=PA,1=PI,2=CO,3=FB,4=DV,5=SH ........:        0.0000
56 - Distance from collimator to detector......cm:        0.0000
57 - ............................................:        0.0000
58 - ............................................:        0.0000
59 - Random collimator movement (0=no)...........:        0.0000
60 - ............................................:        0.0000


Index number.....:
```

Figure A.7 Collimator parameters set to Siemens LEHR collimator.

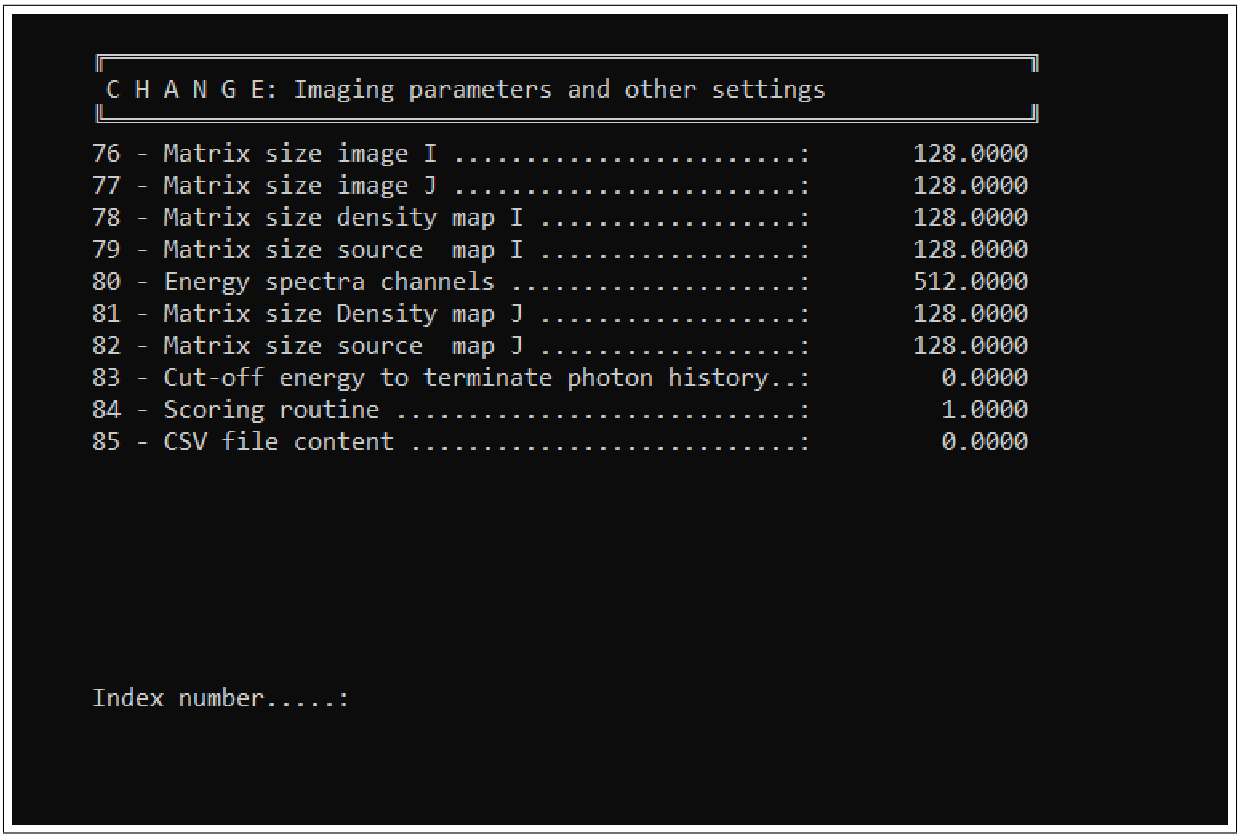

```
 C H A N G E: Imaging parameters and other settings

76 - Matrix size image I ........................:       128.0000
77 - Matrix size image J ........................:       128.0000
78 - Matrix size density map I ..................:       128.0000
79 - Matrix size source  map I ..................:       128.0000
80 - Energy spectra channels ....................:       512.0000
81 - Matrix size Density map J ..................:       128.0000
82 - Matrix size source  map J ..................:       128.0000
83 - Cut-off energy to terminate photon history..:         0.0000
84 - Scoring routine ............................:         1.0000
85 - CSV file content ...........................:         0.0000




Index number.....:
```

Figure A.8 Imaging parameters and matrix size.

REFERENCES

1. W. D. Fraser, “Hyperparathyroidism,” *The Lancet*, vol. 374, pp. 145–158, 7 2009.

2. K. Dandurand, D. S. Ali, and A. A. Khan, “Primary hyperparathyroidism: A narrative review of diagnosis and medical management,” *Journal of Clinical Medicine*, vol. 10, 4 2021.

3. J. A. Wieneke and A. Smith, “Parathyroid adenoma.,” *Head and neck pathology*, vol. 2, pp. 305–8, 12 2008.

4. A. Oral and A. Guvenis, “Improving the detectability of overactive glands in dual-phase parathyroid spect/ct: A monte carlo simulation study,” *Biomedical Physics and Engineering Express*, vol. 7, 7 2021.

5. J. P. Bilezikian, M. L. Brandi, R. Eastell, S. J. Silverberg, R. Udelsman, C. Marcocci, and J. T. Potts, “Guidelines for the management of asymptomatic primary hyperparathyroidism: Summary statement from the fourth international workshop,” vol. 99, pp. 3561–3569, Endocrine Society, 10 2014.

6. A. Ilahi, E. Muco, and T. B. Ilahi, *Anatomy, Head and Neck, Parathyroid.* 2022.

7. P. Ritt, H. Vija, J. Hornegger, and T. Kuwert, “Absolute quantification in spect,” *European Journal of Nuclear Medicine and Molecular Imaging*, vol. 38, 5 2011.

8. P. Ritt, “Recent developments in spect/ct,” *Seminars in Nuclear Medicine*, vol. 52, pp. 276–285, 5 2022.

9. Y. Wang, Y. Liu, N. Li, K. Xu, and W. Zhang, “Quantitative application of dual-phase 99mtc-sestamibi spect/ct imaging of parathyroid lesions: identification of optimal timing in secondary hyperparathyroidism,” *EJNMMI Physics*, vol. 10, 12 2023.

10. H. Lee, J. H. Kim, Y. K. Kang, J. H. Moon, Y. So, and W. W. Lee, “Quantitative single-photon emission computed tomography/computed tomography for technetium pertechnetate thyroid uptake measurement,” *Medicine (United States)*, vol. 95, 7 2016.

11. R. E. Khouli, M. Lodge, M. Zeiger, M. Vranesic, H. Ziessman, and Z. Szabo, “Quantitative spect ct of the parathyroid with suv measurements,” *Journal of Nuclear Medicine*, vol. 56, p. 1645, 5 2015.

12. R. E. Khouli, E. Turkbey, M. Lodge, M. Vranesic, H. Ziessman, D. Spence, X. Ding, A. Vija, and Z. Szabo, “Standardized uptake value based assessment of dual phase parathyroid spect ct: Promising role in equivocal cases,” *Journal of Nuclear Medicine*, vol. 58, p. 101, 5 2017.

13. “Eanm’16,” vol. 43, pp. 1–734, 10 2016.

14. H.-J. Im, I. K. Lee, J. C. Paeng, K. E. Lee, G. J. Cheon, K. W. Kang, J.-K. Chung, and D. S. Lee, “Functional evaluation of parathyroid adenoma using 99mtc-mibi parathyroid spect/ct,” *Nuclear Medicine Communications*, vol. 35, pp. 649–654, 6 2014.

15. H. Y. Suh, H. Y. Na, S. Y. Park, J. Y. Choi, Y. So, and W. W. Lee, “The usefulness of maximum standardized uptake value at the delayed phase of tc-99m sestamibi single-photon emission computed tomography/computed tomography for identification of parathyroid adenoma and hyperplasia,” *Medicine*, vol. 99, p. e21176, 7 2020.

16. M. H. Listewnik, H. Piwowarska-Bilska, K. Safranow, J. Iwanowski, M. LaszczyÅska, M. Chosia, M. Ostrowski, B. Birkenfeld, D. Oszutowska-Mazurek, and P. Mazurek, "Estimation of parameters of parathyroid glands using particle swarm optimization and multivariate generalized gaussian function mixture," *Applied Sciences (Switzerland)*, vol. 9, 11 2019.

17. M. Havel, V. Dedek, M. Kolacek, and M. Formanek, "Quantitative analysis in parathyroid adenoma scintigraphy," *Nuclear Medicine Communications*, vol. 43, pp. 1–7, 1 2022.

18. P. Robin, R. Klein, J. Gardner, B. Ziebarth, S. Bazarjani, S. Razavi, L. S. Zuckier, and W. Zeng, "Quantitative analysis of technetium-99m-sestamibi uptake and washout in parathyroid scintigraphy supports dual mechanisms of lesion conspicuity," *Nuclear Medicine Communications*, vol. 40, pp. 469–476, 5 2019.

19. J. Ma, J. Yang, C. Chen, Y. Lu, Z. Mao, H. Wang, Y. Yang, Z. Li, W. Wang, and L. Teng, "Use of 99mtc-sestamibi spect/ct imaging in predicting the degree of pathological hyperplasia of the parathyroid gland: Semi-quantitative analysis," *Quantitative Imaging in Medicine and Surgery*, vol. 11, pp. 4375–4388, 10 2021.

20. L. Harris, J. Yoo, A. Driedger, K. Fung, J. Franklin, D. Gray, and R. Holliday, "Accuracy of technetium-99m spect-ct hybrid images in predicting the precise intraoperative anatomical location of parathyroid adenomas," *Head and Neck*, vol. 30, pp. 509–517, 4 2008.

21. S. Razavi, B. Ziebarth, R. Klein, and W. Zeng, "Dual time-point quantitative spect-ct parathyroid imaging using a single computed tomography," *Nuclear Medicine Communications*, vol. 39, pp. 3–9, 1 2018.

22. M. D'Arienzo, M. Cazzato, M. L. Cozzella, M. Cox, M. D'Andrea, A. Fazio, A. Fenwick, G. Iaccarino, L. Johansson, L. Strigari, S. Ungania, and P. D. Felice, "Gamma camera calibration and validation for quantitative spect imaging with 177lu," *Applied Radiation and Isotopes*, vol. 112, pp. 156–164, 6 2016.

23. M. Ljungberg, "Absolute quantitation of spect studies," *Seminars in Nuclear Medicine*, vol. 48, pp. 348–358, 7 2018.

24. A. Maier, S. Steidl, and V. Christlein, *Medical Imaging Systems*, vol. 11111. Springer International Publishing, 2018.

25. B. F. Hutton, "The origins of spect and spect/ct," *European Journal of Nuclear Medicine and Molecular Imaging*, vol. 41, 2014.

26. L. Livieratos, "Technical pitfalls and limitations of spect/ct," *Seminars in Nuclear Medicine*, vol. 45, pp. 530–540, 11 2015.

27. A. J. Einstein, R. Blankstein, H. Andrews, M. Fish, R. Padgett, S. W. Hayes, J. D. Friedman, M. Qureshi, H. Rakotoarivelo, P. Slomka, R. Nakazato, S. Bokhari, M. D. Carli, and D. S. Berman, "Comparison of image quality, myocardial perfusion, and left ventricular function between standard imaging and single-injection ultra-low-dose imaging using a high-efficiency spect camera: The millisievert study," *Journal of Nuclear Medicine*, vol. 55, pp. 1430–1437, 9 2014.

28. L. Imbert, S. Poussier, P. R. Franken, B. Songy, A. Verger, O. Morel, D. Wolf, A. Noel, G. Karcher, and P. Y. Marie, "Compared performance of high-sensitivity cameras dedicated to myocardial perfusion spect: A comprehensive analysis of phantom and human images," *Journal of Nuclear Medicine*, vol. 53, pp. 1897–1903, 12 2012.

29. H. Wieczorek, A. Goedicke, F. Edstrom, C. Degenhardt, H. Botterweck, and R. Bippus, “Collimator spatial resolution,” in *IEEE Nuclear Science Symposium Conference Record, 2005*, vol. 3, pp. 5 pp.–1721, Oct 2005.

30. P. Ritt, J. Sanders, and T. Kuwert, “Spect/ct technology,” *Clinical and Translational Imaging*, vol. 2, pp. 445–457, 12 2014.

31. J. Cui, G. Pratx, B. Meng, and C. S. Levin, “Distributed mlem: An iterative tomographic image reconstruction algorithm for distributed memory architectures,” *IEEE Transactions on Medical Imaging*, vol. 32, pp. 957–967, 2013.

32. D. L. Bailey and K. P. Willowson, “Quantitative spect/ct: Spect joins pet as a quantitative imaging modality,” *European Journal of Nuclear Medicine and Molecular Imaging*, vol. 41, 2014.

33. D. L. Bailey and K. P. Willowson, “An evidence-based review of quantitative spect imaging and potential clinical applications,” *Journal of Nuclear Medicine*, vol. 54, pp. 83–89, 1 2013.

34. J. A. Patton and T. G. Turkington, “Spect/ct physical principles and attenuation correction,” *Journal of Nuclear Medicine Technology*, vol. 36, pp. 1–10, 3 2008.

35. V. Changizi, A. Takavar, A. Babakhani, and M. Sohrabi, “Scatter correction for heart spect images using tew method,” *Journal of Applied Clinical Medical Physics*, vol. 9, pp. 136–140, 2008.

36. M. Ashoor, A. Asgari, A. Khorshidi, and A. Rezaei, “Evaluation of compton attenuation and photoelectric absorption coefficients by convolution of scattering and primary functions and counts ratio on energy spectra,” *Indian Journal of Nuclear Medicine*, vol. 30, pp. 239–247, 7 2015.

37. K. Ogawa, Y. Harata, T. Ichihara, A. Kubo, and S. Hashimoto, “A practical method for position-dependent compton-scatter correction in single photon emission ct,” *IEEE Transactions on Medical Imaging*, vol. 10, pp. 408–412, 1991.

38. K. A. Blokland, W. H. D. V. T. N. Cappel, B. L. V. Eck-Smit, and E. K. Pauwels, “Scatter correction on its own increases image contrast in tl-201 myocardium perfusion scintigraphy, but does it also improve diagnostic accuracy?,” *Annals of Nuclear Medicine*, vol. 17, pp. 725–731, 2003.

39. R. L. Harrison, “Introduction to monte carlo simulation,” vol. 1204, pp. 17–21, 2009.

40. M. T. B. Toossi, J. P. Islamian, M. Momennezhad, M. Ljungberg, and S. H. Naseri, “Simind monte carlo simulation of a single photon emission ct.,” *Journal of medical physics*, vol. 35, pp. 42–7, 1 2010.

41. F. H. Fahey, K. Grogg, and G. E. Fakhri, “Use of monte carlo techniques in nuclear medicine.,” *Journal of the American College of Radiology : JACR*, vol. 15, pp. 446–448, 3 2018.

42. H. Zaidi, “Relevance of accurate monte carlo modeling in nuclear medical imaging,” *Medical Physics*, vol. 26, pp. 574–608, 1999.

43. J. Wevrett, A. Fenwick, J. Scuffham, and A. Nisbet, “Development of a calibration protocol for quantitative imaging for molecular radiotherapy dosimetry,” *Radiation Physics and Chemistry*, vol. 140, pp. 355–360, 11 2017.

44. A. Oral and A. Guvenis, “A digital platform for simulating the accurate detectability of overactive parathyroid glands in spect/ct imaging,” Institute of Electrical and Electronics Engineers Inc., 10 2019.

45. V. Tunninen, T. Kauppinen, and H. Eskola, “Physical characteristics of collimators for dual-isotope imaging with 99mtc and 123i,” vol. 65, pp. 245–249, Springer Verlag, 2017.

46. A. N. Vasavada, J. Danaraj, and G. P. Siegmund, “Head and neck anthropometry, vertebral geometry and neck strength in height-matched men and women,” *Journal of Biomechanics*, vol. 41, pp. 114–121, 2008.

47. M. Ljungberg, “The simind monte-carlo program.”

48. J. Gustafsson, G. Brolin, and M. Ljungberg, “Monte carlo-based spect reconstruction within the simind framework,” *Physics in Medicine Biology*, vol. 63, p. 245012, 12 2018.

49. M. Ljungberg, K. Sjögreen, X. Liu, E. Frey, Y. Dewaraja, and S.-E. Strand, “A 3-dimensional absorbed dose calculation method based on quantitative spect for radionuclide therapy: Evaluation for 131i using monte carlo simulation,” *Journal of Nuclear Medicine*, vol. 43, p. 1101, 8 2002.

50. M. Ljungberg and K. Sjögreen-Gleisner, “The accuracy of absorbed dose estimates in tumours determined by quantitative spect: A monte carlo study,” vol. 50, pp. 981–989, 8 2011.

51. D. Minarik, K. S. Gleisner, and M. Ljungberg, “Evaluation of quantitative 90y spect based on experimental phantom studies,” *Physics in Medicine and Biology*, vol. 53, pp. 5689–5703, 10 2008.

52. T. Merlin, S. Stute, D. Benoit, J. Bert, T. Carlier, C. Comtat, M. Filipovic, F. Lamare, and D. Visvikis, “Castor: a generic data organization and processing code framework for multi-modal and multi-dimensional tomographic reconstruction,” *Physics in Medicine Biology*, vol. 63, p. 185005, 9 2018.

53. J. K. Bong, H. K. Son, J. D. Lee, and H. J. Kim, “Improved scatter correction for spect images: A monte carlo study,” *IEEE Transactions on Nuclear Science*, vol. 52, pp. 1263–1270, 2005.

54. A. Halty, J. N. Badel, O. Kochebina, and D. Sarrut, “Image-based spect calibration based on the evaluation of the fraction of activity in the field of view,” *EJNMMI Physics*, vol. 5, 12 2018.

55. A. Frezza, C. Desport, C. Uribe, W. Zhao, A. Celler, P. DesprÃ©s, and J. M. Beauregard, “Comprehensive spect/ct system characterization and calibration for 177lu quantitative spect (qspect) with dead-time correction,” *EJNMMI Physics*, vol. 7, 12 2020.

56. A. Fedorov, R. Beichel, J. Kalpathy-Cramer, J. Finet, J.-C. Fillion-Robin, S. Pujol, C. Bauer, D. Jennings, F. Fennessy, M. Sonka, J. Buatti, S. Aylward, J. V. Miller, S. Pieper, and R. Kikinis, “3d slicer as an image computing platform for the quantitative imaging network.,” *Magnetic resonance imaging*, vol. 30, pp. 1323–41, 11 2012.

57. L. E. Carvalho, A. C. Sobieranski, and A. von Wangenheim, “3d segmentation algorithms for computerized tomographic imaging: a systematic literature review,” *Journal of Digital Imaging*, vol. 31, pp. 799–850, 12 2018.

58. Z. Jun and H. Jinglu, “Image segmentation based on 2d otsu method with histogram analysis,” vol. 6, pp. 105–108, 2008.

59. C. H. Bindu, “An improved medical image segmentation algorithm using otsu method,” 2009.

60. C. H. Bindu and K. S. Prasad, “An efficient medical image segmentation using conventional otsu method,” 2012.

61. J. J. V. Griethuysen, A. Fedorov, C. Parmar, A. Hosny, N. Aucoin, V. Narayan, R. G. Beets-Tan, J. C. Fillion-Robin, S. Pieper, and H. J. Aerts, “Computational radiomics system to decode the radiographic phenotype,” *Cancer Research*, vol. 77, pp. e104–e107, 11 2017.

62. A. Fedorov, D. Clunie, E. Ulrich, C. Bauer, A. Wahle, B. Brown, M. Onken, J. Riesmeier, S. Pieper, R. Kikinis, J. Buatti, and R. R. Beichel, “Dicom for quantitative imaging biomarker development: A standards based approach to sharing clinical data and structured pet/ct analysis results in head and neck cancer research,” *PeerJ*, vol. 2016, 2016.

63. V. R. R. Jose, “Percentage and relative error measures in forecast evaluation,” *Operations Research*, vol. 65, no. 1, pp. 200–211, 2017.

64. A. B. Hwang, B. L. Franc, G. T. Gullberg, and B. H. Hasegawa, “Assessment of the sources of error affecting the quantitative accuracy of spect imaging in small animals,” *Physics in Medicine and Biology*, vol. 53, pp. 2233–2252, 5 2008.

65. J. Zeintl, A. H. Vija, A. Yahil, J. Hornegger, and T. Kuwert, “Quantitative accuracy of clinical 99mtc spect/ct using ordered-subset expectation maximization with 3-dimensional resolution recovery, attenuation, and scatter correction,” *Journal of Nuclear Medicine*, vol. 51, pp. 921–928, 6 2010.

66. S. Bashir, S. Fatima, A. Ammar, and A. Khawar, “Quantitative analysis in parathyroid scintigraphy: [99mtc]tc-mibi spect/ct a tool for noninvasive characterization of parathyroid lesions,” *Clinical and Translational Imaging*, 2023.

67. R. Pagnanelli and S. Borges-Neto, “Technical aspects of resolution recovery reconstruction,” *Journal of Nuclear Cardiology*, vol. 23, pp. 149–152, 2016.

68. H. J. Kim, J. I. Bang, J. Y. Kim, J. H. Moon, Y. So, and W. W. Lee, “Novel application of quantitative single-photon emission computed tomography/computed tomography to predict early response to methimazole in gravesâ disease,” *Korean Journal of Radiology*, vol. 18, pp. 543–550, 2017.